Supplementary Information

Controlled phase and structure engineering-driven unique dielectric behavior enabling tailored electromagnetic attenuation

Sihao Dou[1], Yunfei He[1], Yuxiang Zheng[1], Yuefeng Yan[2], Zhiyuan Dan[1], Long Ma[1], Minghao Yang[1], Dongdong Liu[1], Xiaoxiao Huang[2,3], Bo Zhong[1,4]

[1] School of Materials Science and Engineering, Harbin Institute of Technology, Weihai 264209, China

[2] School of Materials Science and Engineering, Harbin Institute of Technology, Harbin, 150001, China

[3] MIIT Key Laboratory of Advanced Structural-Functional Integration Materials & Green Manufacturing Technology, Harbin, 150001, China

[4] State Key Laboratory of Precision Welding & Joining of Materials and Structures, Harbin, 150001, China

Corresponding author:

Dongdong Liu, liuddhit@hit.edu.cn

Bo Zhong, zhongbo@hit.edu.cn

Experimental Section

Preparation of CZ, FCZ*x*, and FCZ4-*y*

1) Raw materials

Zinc acetate dihydrate, cobalt nitrate hexahydrate, 2-Methylimidazole, and iron(III) acetylacetonate were purchased from Shanghai Macklin Biochemical Technology Co., Ltd, China. All the reagents were analytical grade and used without further purification. All solutions were prepared using deionized water.

2) Synthesis of CZ-Z and FCZ-Z*x*

12 mmol of $Zn(OAc)_2 \cdot 2H_2O$ and 12 mmol of $Co(NO_3)_2 \cdot 6H_2O$ were dissolved in 80 mL of deionized water and stirred for a while to obtain solution A. 100 mmol 2-methylimidazole was dissolved in 40 mL of deionized water and stirred for a while to obtain solution B. Then, solution B was poured into solution A and aged for 48 hours at room temperature. The Co/Zn-ZIF (CZ-Z) precursors were obtained by centrifugation, washed with deionized water, and then freeze-drying for 48 hours. Fe-Co/Zn-ZIF*x* (*x*=1, 2, 3, 4, 5, and 6) precursors were obtained by adding $Fe(acac)_3$ with different amounts (0.6 mmol, 1.2 mmol, 1.8 mmol, 2.4 mmol, 3.0 mmol, and 3.6 mmol, respectively) to solution A. Other preparation processes were the same. The obtained precursors were labeled as FCZ-Z1, FCZ-Z2, FCZ-Z3, FCZ-Z4, FCZ-Z5 and FCZ-Z6, respectively. For comparison, monometallic Zn-ZIF (MZ-Z, 24 mmol of zinc acetate and zero mmol of cobalt nitrate) and Fe-Zn-ZIF (FZ-Z, 2.4 mmol of $Fe(acac)_3$) were obtained by the same process. Monometallic Co-ZIF (MC-Z, zero mmol of zinc acetate and 24 mmol of cobalt nitrate) and Fe-Co-ZIF (FC-Z, 2.4 mmol of $Fe(acac)_3$) were also prepared using the same process.

3) Synthesis of CZ and FCZ*x*

To obtain CZ and FCZ*x*, the CZ-Z and FCZ-Z*x* were treated by annealing at 600 °C for 3 hours at a heating rate of 2 °C min^{-1} in nitrogen (N_2), respectively. The same heat treatment process was also applied to MZ-Z or MC-Z and FZ-Z or FC-Z to synthesize Zn@NC (MZ) or Co@NC (MC) and Fe-Zn@NC (FZ) or Fe-Co@NC (FC).

4) Synthesis of FCZ4-*y*

The FCZ4 was processed by annealing at different temperatures (500 °C, 700 °C, 800 °C, 900 °C, and 1000 °C) for three hours at a heating rate of 2 °C min^{-1} in N_2 to obtain FCZ4-*y* (*y*=5, 7, 8, 9, and 10). The specific sample naming rules were shown in **Table S1**.

Characterization

Structure, physical, and chemical properties: Field emission scanning electron microscopy (SEM, Merlin Compact, Zeiss, Germany) and high-resolution transmission electron microscopy (TEM, FEI Talos F200x, America) with an energy dispersive X-ray spectroscopy (EDS, Super-X) were employed to appraise the morphologies and components of the samples. The crystal structure of the samples was determined using the powder X-ray diffraction (XRD, D8 Advanced, Bruker, Germany) technique with Cu Kα radiation (λ = 0.15418 nm) at a scanning voltage of 30 kV and a scanning range of 5° to 90°. X-ray photoelectron spectroscopy (XPS, Thermo Scientific K-Spin-up, Thermo Fisher, America) measurements were carried out to analyze the chemical composition and valence state of the samples. Thermogravimetry (TG, FTA4495F, Netzsch, Germany) was employed to analyze the thermal stability of materials. The specific surface areas and porosity of the powders were evaluated using N2 gas adsorption-desorption isotherms at 77 K, as determined by the Brunauer-Emmett-Teller technique (Bet, ASAP2460, Mike, America). Inductively coupled plasma optical emission spectrometry (ICP-OES, Agilent 5110, America) was utilized to determine the elemental content of materials. A vibrating sample magnetometer (VSM, LakeShore 7404, America) was employed to measure magnetization (*M*) versus applied magnetic field (*H*) at room temperature. The conductivity (σ) of the sample with 100 wt% filler loading was measured by a four-point probe powder resistivity tester. Meanwhile, the conductivity of the coaxial ring (50 wt% filler loading) was tested with an electrochemical workstation (CHI 660D, Shanghai Chenhua Instrument, China). Electronic paramagnetic resonance (EPR, EMXplus-6/1, Bruker, Germany) was employed to obtain information on vacancy defects. Photoluminescence spectroscopy

(PL, FLS1000, Edinburgh, Britain, λ = 275 nm) was utilized to determine the defect level of the samples. Raman spectrometer (inVia, Renishaw, UK) was used to acquire information on the degree of crystallization and graphitization of carbon in composites.

Electromagnetic wave absorption performance test

The powder was uniformly mixed with paraffin in a mass proportion of 50:50, respectively, and subsequently compacted into coaxial rings with an outer diameter of 7.00 mm and an inner diameter of 3.04 mm. Electromagnetic (EM) parameters were obtained by the microwave vector network analyzer (Agilent N5245A, America). Furthermore, to eliminate potential errors caused by instrumental variations or operational inconsistencies, as well as to verify the reliability and repeatability of the composites, new EM parameters were acquired in another microwave vector network analyzer (Agilent E5071C, America, provided and tested by Scientific Compass, Hangzhou Research Interest Information Technology Co., Ltd). According to the transmission line theory, the required physical quantities could be calculated through electromagnetic parameters, frequency, and thickness, as follows:

The equation of complex permittivity and complex permeability was as follows:

$$\varepsilon_r = \varepsilon^{''} - j\varepsilon^{'} \tag{1}$$

$$\mu_r = \mu^{''} - j\mu^{'} \tag{2}$$

Where ε_r was the complex permittivity, ε' was the real part of the permittivity, ε'' was the imaginary part of the permittivity, μ_r was the complex permeability, μ' was the real part of the permeability, μ'' was the imaginary part of the permeability.

The normalized input impedance (Z) was expressed as follows:

$$Z = \left|\frac{Z_{in}}{Z_o}\right| = \sqrt{\frac{\mu_r}{\varepsilon_r}} \tan h\left[j\left(\frac{2\pi f d}{c}\right)\sqrt{\mu_r \varepsilon_r}\right] \tag{3}$$

$$Z_0 = \sqrt{\frac{\mu_0}{\varepsilon_0}} \tag{4}$$

Where Z_{in} was the material impedance, Z_0 was the air impedance, μ_0 was the permeability of vacuum ($4\pi\times10^{-7}$ N A^{-2}), ε_0 was the vacuum permittivity (8.85×10^{-12} F m^{-1}), c was the light speed, f was the frequency, and d was the material thickness.

The reflection loss (RL) value was calculated using the following equation:

$$RL = 20\,log\left|\frac{Z_{in} - Z_o}{Z_{in} + Z_o}\right| \tag{5}$$

The equation for calculating the attenuation constant (AC) was as follows:

$$AC = \frac{\sqrt{2}\pi f}{c}\sqrt{\mu''\varepsilon'' - \mu'\varepsilon' + \sqrt{(\mu''\varepsilon'' - \mu'\varepsilon')^2 + (\mu'\varepsilon'' + \mu''\varepsilon')^2}} \tag{6}$$

According to the theory of Debye, ε' was related to polarization, while ε'' depended on the conduction loss (ε_c'') and polarization loss (ε_p'') comprehensive contribution. Its equation was as follows:

$$\varepsilon' = \varepsilon_\infty + \frac{(\varepsilon_s - \varepsilon_\infty)}{1 + (2\pi f)^2\tau^2} \tag{7}$$

$$\varepsilon'' = \varepsilon_p'' + \varepsilon_c'' = (\varepsilon_s - \varepsilon_\infty)\frac{2\pi f\tau}{1 + (2\pi f)^2\tau^2} + \frac{\sigma}{2\pi f\varepsilon_0} \tag{8}$$

$$\varepsilon_p'' = (\varepsilon_s - \varepsilon_\infty)\frac{2\pi f\tau}{1 + (2\pi f)^2\tau^2} \tag{9}$$

$$\varepsilon_c'' = \frac{\sigma}{2\pi f\varepsilon_0} \tag{10}$$

Where σ was the electrical conductivity, ε_s was the static permittivity, ε_∞ was the infinite frequency permittivity, and τ was the relaxation time.

The modified Havriliak-Negami model was employed to fit the complex permittivity curve to acquire more information about the relaxation time in it, as shown in the following equation:

$$\varepsilon_r = \varepsilon_\infty + \frac{\varepsilon_s - \varepsilon_\infty}{[1 + (i\omega\tau)^\alpha]^\beta} - i\frac{\sigma}{\omega\varepsilon_0} \tag{11}$$

Where α denoted the symmetrical broadening coefficient governing the relaxation time, and β represented the asymmetrical coefficient modulating the loss peak. Based on equation (11), we developed corresponding Python code to fit the relevant parameters, including static permittivity (ε_s), optical frequency permittivity (ε_∞), relaxation time (τ), conductivity (σ), and relaxation factors (α and β). The Python code used for this purpose is shown in **Note S5**.

To analyze the polarization relaxation process, the ε'-ε'' curve was used to describe the Cole-Cole semicircle. According to the theory of Debye, the ε' and ε'' relationship could be expressed as follows:

$$\left(\varepsilon' - \frac{\varepsilon_s + \varepsilon_\infty}{2}\right)^2 + \left(\varepsilon''\right)^2 = \left(\frac{\varepsilon_s + \varepsilon_\infty}{2}\right)^2 \tag{12}$$

To elucidate the mechanism governing the low-frequency shift of absorption peaks with increasing thickness and high-frequency shift with enhanced material filling ratio, a quarter wavelength model was employed to characterize the correlation between the peak absorption frequency (f_m) and the optimized thickness (t_m), as shown in the equation below:

$$t_m = \frac{n\lambda}{4} = \frac{nc}{4f_m\sqrt{|\mu_r||\varepsilon_r|}} \ (n = 1, 3, 5, \ldots) \tag{13}$$

Electromagnetic shielding performance test

The powder was uniformly mixed with paraffin in a mass proportion of 50:50, respectively, and subsequently compacted into coaxial rings with an outer diameter of 7.00 mm and an inner diameter of 3.04 mm. The S-parameters (S_{11}, S_{22}, S_{12}, and S_{21}) were obtained by the microwave vector network analyzer (Agilent N5245A, America). By applying the transmission line theory, these parameters could be converted into EMI shielding coefficients, namely, transmittance (T), reflectance (R), and absorbance (A).

The specific equations were as follows:

$$R = |S_{11}|^2 = |S_{22}|^2 \tag{14}$$

$$T = |S_{12}|^2 = |S_{21}|^2 \tag{15}$$

$$1 = A + R + T \tag{16}$$

Another parameter frequently used to evaluate shielding performance was the SE, referred to as total EMI shielding effectiveness (SE_T). Also, shielding effectiveness by reflection (SE_R) and absorption (SE_A) could be obtained from S-parameters. The equations were shown below:

$$SE_T = 10\log\left(\frac{1}{T}\right) = 10\log\left(\frac{1}{|S_{12}|^2}\right) \tag{17}$$

$$SE_R = 10\log\left(\frac{1}{1-R}\right) = 10\log\left(\frac{1}{1-|S_{11}|^2}\right) \tag{18}$$

$$SE_A = 10\log\left(\frac{1-R}{T}\right) = 10\log\left(\frac{1-|S_{11}|^2}{|S_{12}|^2}\right) \tag{19}$$

Simulation

Plane RCS simulation with CST Studio Suite 2022

A square model measuring 180 × 180 mm^2 was constructed with an absorbing layer of 2.03 mm and a perfect electric conductor (PEC) layer of 1.0 mm. The excitation source was a plane wave, and the spherical coordinate angles θ and φ determined the direction of the scattered EMW. The specific model diagram was shown in Fig. S56. A monitoring frequency of 17.92 GHz was selected. The value of RCS was calculated using the following equation:

$$\sigma\ (dB\ m^2) = 10log\left[\frac{4\pi S}{\lambda^2}\left|\frac{E_s}{E_i}\right|^2\right] \quad (20)$$

Where S represented the area of the simulated plate, λ denoted the wavelength of the incident electromagnetic wave, E_s stood for the emitted electric field strength, and E_i was the received electric field strength. The low scattered signal strength in the final simulation corresponded to high EMW absorption properties.

Electromagnetic power loss density simulation with COMSOL

The electromagnetic power loss density was calculated using COMSOL Multiphysics version 6.2. The frequency selected for the computational simulation was 17.92 GHz. The corresponding model and dimensions referred to the morphology and dimensions in the SEM and TEM images.

Density functional theory (DFT) calculation:

DFT calculations were performed using the Cambridge Serial Total Energy Package (CASTEP) in the Materials Studio software. The exchange-correlation energies were dealt with using generalized gradient approximation-Perdew-Bruke-Ernzerhof (GGA-PBE) with ultrasoft pseudopotentials. The kinetic cutoff energy of 900 eV was chosen for plane-wave expansion. K-point in the Brillouin zone was sampled with a value of 8×8×8. The electronic iterative convergence criterion for structure optimization and energy calculations was $1x10^{-6}$ eV $atom^{-1}$ for self-consistent fields (SCF). All the structures were relaxed until the residual forces on the atoms declined to less than 0.03 eV $Å^{-1}$. The collinear mode under spin polarization was turned on for magnetic systems.

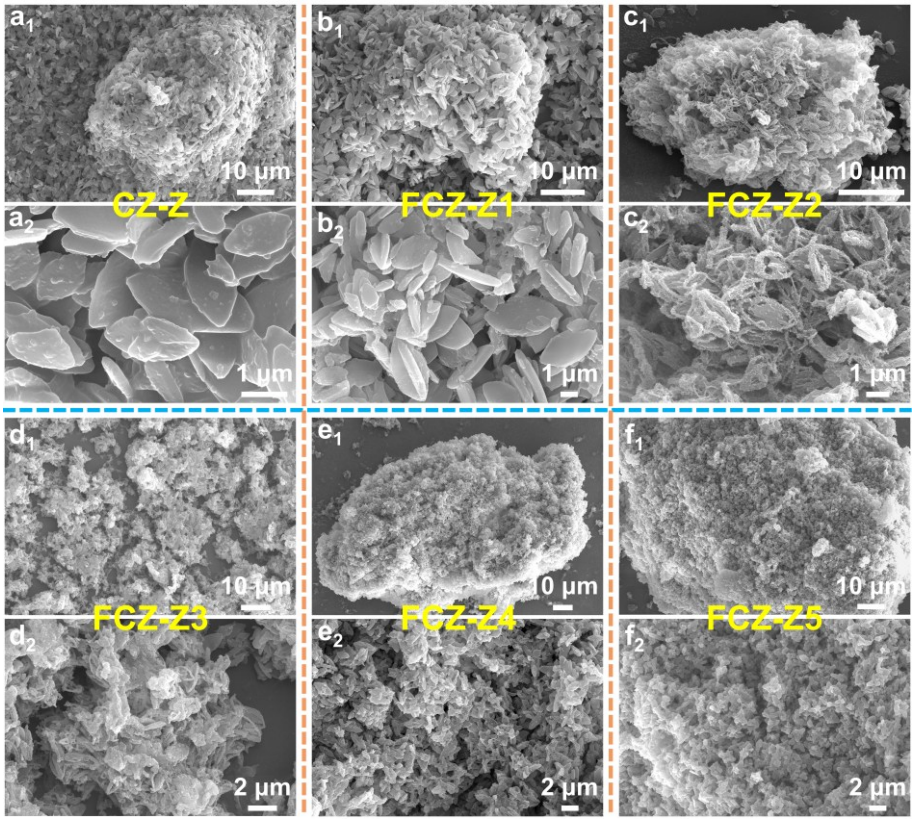

Fig. S1 SEM images of a) CZ-Z, b) FCZ-Z1, c) FCZ-Z2, d) FCZ-Z3, e) FCZ-Z4, and f) FCZ-Z5.

i) The CZ-Z precursor exhibited a leaf-like architecture with a specific thickness. This unique structure might arise from the anisotropic crystal growth governed by asymmetric ligand coordination. ii) The FCZ-Z1 precursor demonstrated a well-defined leaf-like morphology, with initial self-assembly and structural interpenetration features observed. This phenomenon could be principally attributed to the establishment of structurally reinforced Fe-Co-Zn ternary coordination nodes coupled with the augmented metal-ligand bonding strength derived from the elevated charge density characteristic of Fe^{3+}. iii) The FCZ-Z2 precursor framework exhibited a leaf-like structure with pronounced micrometer-scale pores owing to edge corrosion and dissolution. Meanwhile, it demonstrated an enhanced tendency for interlamellar assembly with mutually interpenetrating configurations. iv) Continuous agitation progressively diminished the morphological distinguishability in the precursor with increasing Fe^{3+} content. Nevertheless, pyrolytic treatment maintained the precursor's

structural integrity while achieving enhanced outline definition.

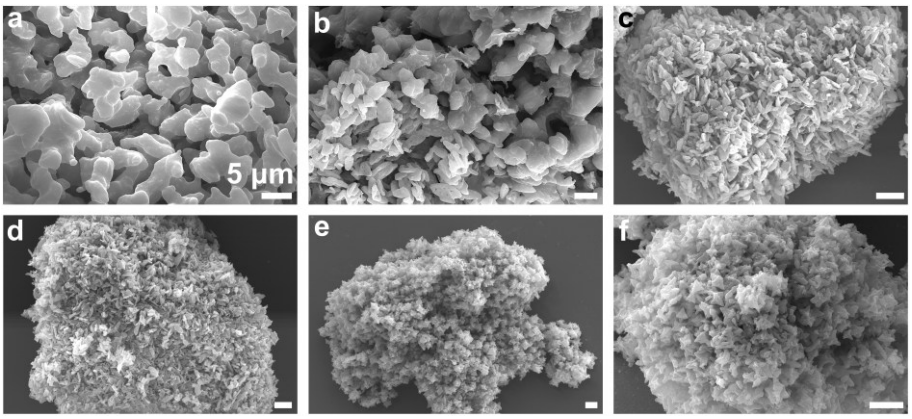

Fig. S2 SEM images of a) CZ, b) FCZ1, c) FCZ2, d) FCZ3, e) FCZ4, and f) FCZ5 (all images were on a five µm scale bar).

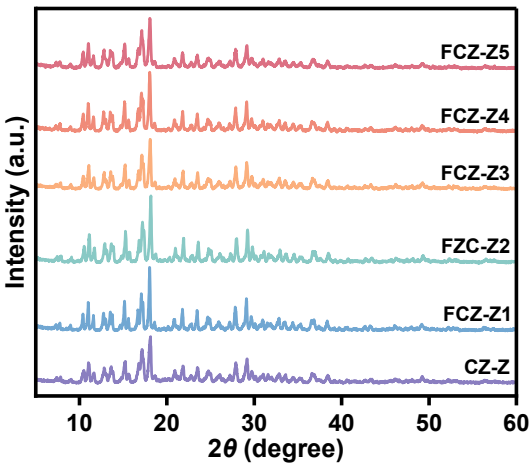

Fig. S3 XRD patterns of CZ-Z and FCZ-Z*x* precursors.

The X-ray diffraction (XRD) analysis revealed that introducing Fe^{3+} into the precursor system did not induce any detectable phase transformations, as evidenced by the absence of emergent diffraction peak features and the preservation of original peak intensity profiles.

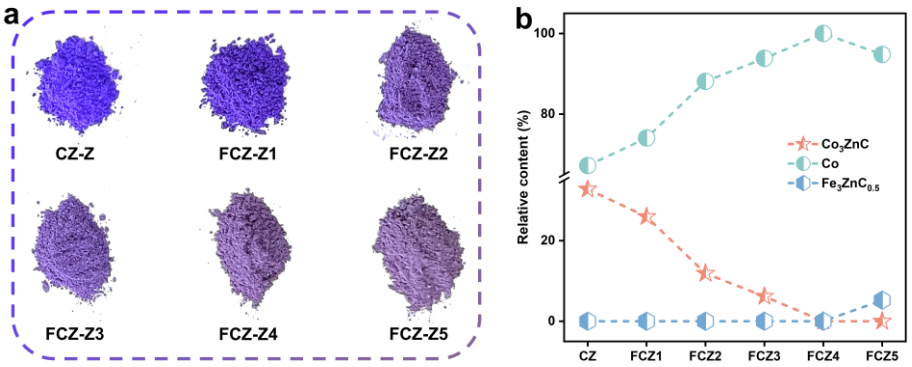

Fig. S4 a) Digital photos of CZ-Z, FCZ-Z1, FCZ-Z2, FCZ-Z3, FCZ-Z4, and FCZ-Z5 precursors (each sample was approximately 1 cm wide). b) The relative content of different components obtained from XRD.

As the Fe^{3+} content increased, the precursor gradually became lighter from its original purple color, indicating that Fe^{3+} had been successfully incorporated into the bimetallic MOF system.

Semi-quantitative XRD analysis indicated that the concentration of Co_3ZnC progressively decreased with the introduction of Fe^{3+}, confirming the inhibitory effect of Fe^{3+} on the nucleation of Co_3ZnC.

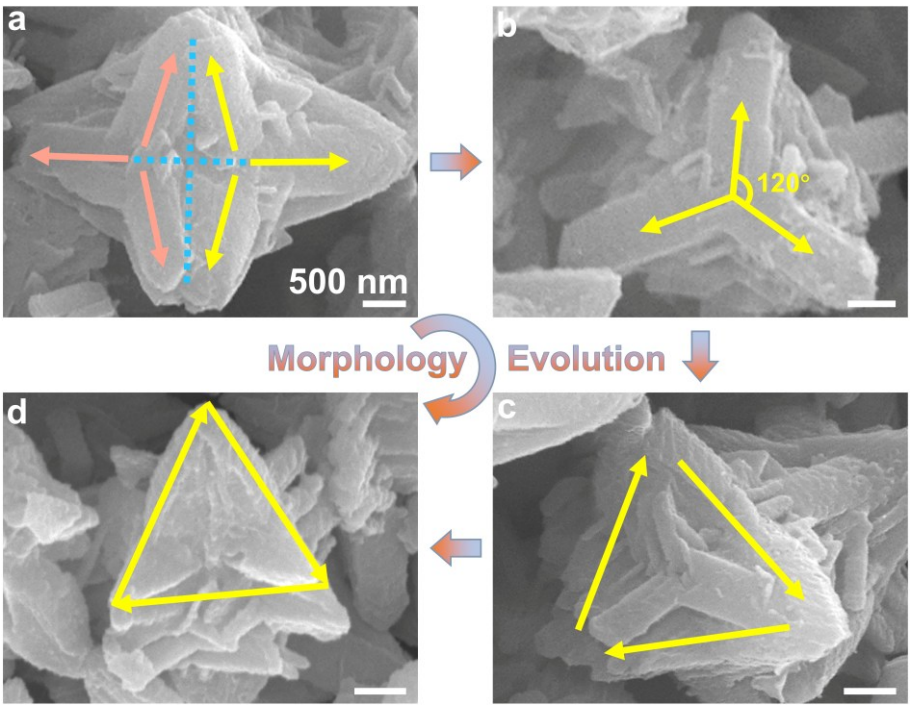

Fig. S5 SEM images of FCZ4 (all images were on a 500 nm scale bar).

The leaf-like structures exhibited mutual cropping and splitting behaviors as the self-assembly approached saturation. Thus, various configurations were observed in FCZ4. This was the process of progressive development and evolution of the architecture, which also served as the foundational framework for understanding the emergence of the stacked star-like structure that formed in FCZ5, as detailed in the following description: a) The leaf-like structures were cropped from one another, resulting in the leaves being split along both axes (blue dashed line) of their surface. b) A leaf was divided into four symmetrical rectangular-like structures, where two rectangles were separated along the direction of the long axis of the surface, and one rectangle from another disconnected leaf was assembled to form a triangular boomerang-like structure, arranged at angles of 120° to each other. c) The material extended outward into a triangular-like architecture as it progressively grew and blended into one another. Nevertheless, the triangular boomerang-like structure was still visible at this point. d) The material essentially formed a triangle-shaped morphology, providing the basis for star-like structures in FCZ5.

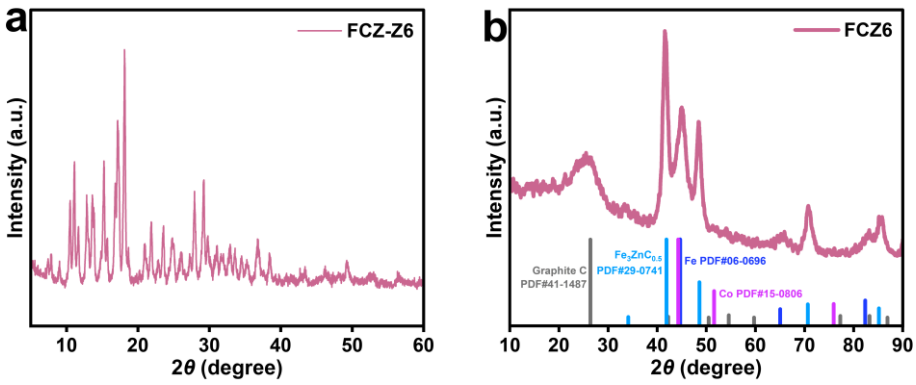

Fig. S6 XRD patterns of a) FCZ-Z6 and b) FCZ6.

The crystal structure of the FCZ-Z6 precursor showed no notable alterations. New diffraction peaks at 33.4°, 70.2°, and 84.6° in FCZ6, assigned to the (110), (220), and (311) crystal planes of $Fe_3ZnC_{0.5}$, respectively, confirmed the absence of the Co_3ZnC phase and the existence of the $Fe_3ZnC_{0.5}$ phase. The intensity of the diffraction peaks at 41.7° and 48.4°, belonging to the (111) and (200) crystal planes of $Fe_3ZnC_{0.5}$, respectively, was strengthened compared to that of FCZ5. The intensity of the diffraction peaks at 65.4° and 82.8°, corresponding to the (200) and (211) crystal planes of Fe, respectively, was also enhanced compared to that of FCZ5.

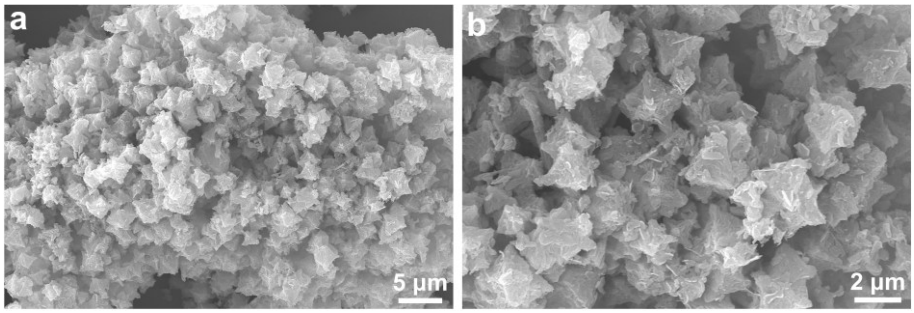

Fig. S7 SEM images of FCZ6.

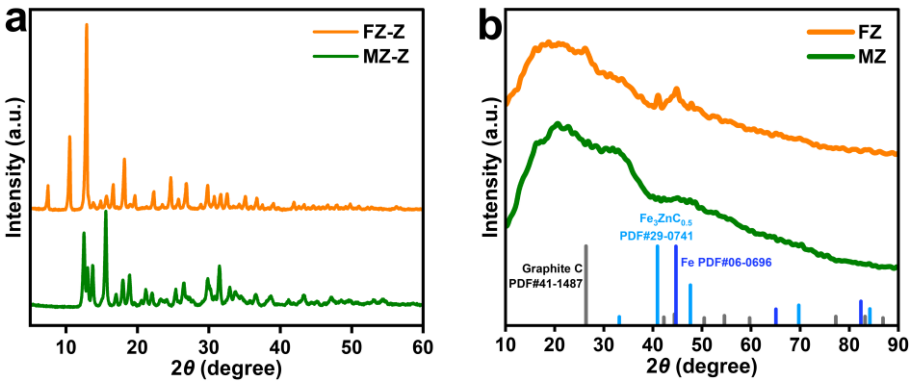

Fig. S8 XRD patterns of a) MZ-Z and FZ-Z, and b) MZ and FZ.

In comparison to the MZ-Z precursor, several new diffraction peaks appeared in the FZ-Z precursor, indicating the successful introduction of Fe^{3+} and the alteration of the crystal structure and chemical composition of the precursor. Besides, observing that the mixed solution rapidly changed from its original white color to an orange-yellow hue upon adding $Fe(acac)_3$ suggested a violent chemical reaction. Following pyrolysis, only broad peaks located around 23.0° and 44.4°, corresponding to the (002) and (101) crystal planes of graphitic carbon, respectively, were detected in MZ. The absence of diffraction peaks for Zn species may be due to its dispersion in the carbon matrix in amorphous phases, which conventional XRD techniques cannot detect. The new diffraction peaks in FZ could be ascribed to the metallic Fe and $Fe_3ZnC_{0.5}$ phases. Specifically, the diffraction peak situated at 44.8° belonged to the (110) crystal plane of metallic Fe, while the peaks located at 41.1° and 47.9° were associated with the (111) and (200) crystal planes of $Fe_3ZnC_{0.5}$, respectively.

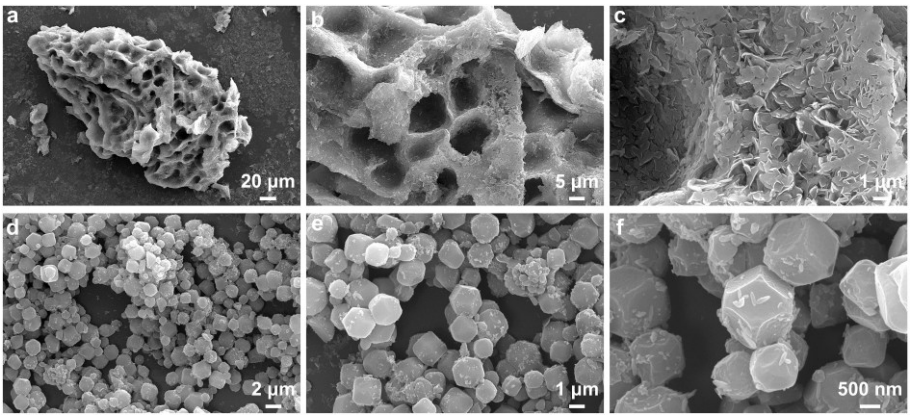

Fig. S9 SEM images of a-c) MZ-Z and d-f) FZ-Z.

The MZ-Z precursor exhibited a block structure with porous features, while Fe^{3+} incorporation shifted the topology of ZIF to a dodecahedral-like configuration.

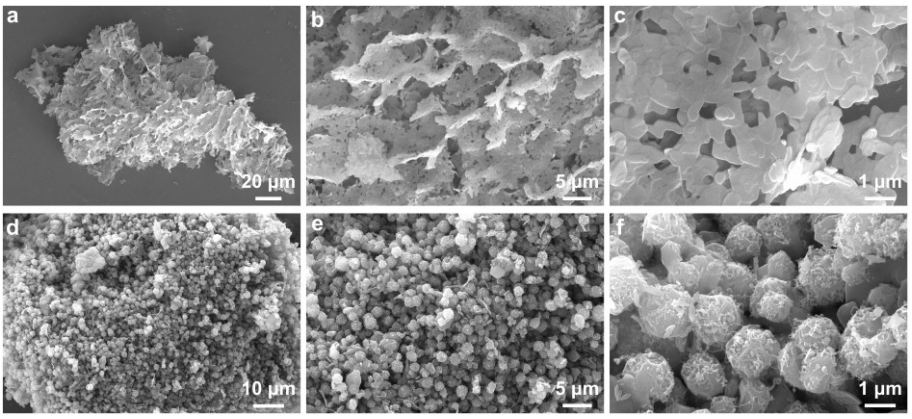

Fig. S10 SEM images of a-c) MZ and d-f) FZ.

In contrast to the MZ-Z precursor, the structure of MZ collapsed into a porous nanosheet architecture, whereas the Fe^{3+}-introduced FZ essentially retained the framework of the precursor, demonstrating a spherical-like polyhedral structure.

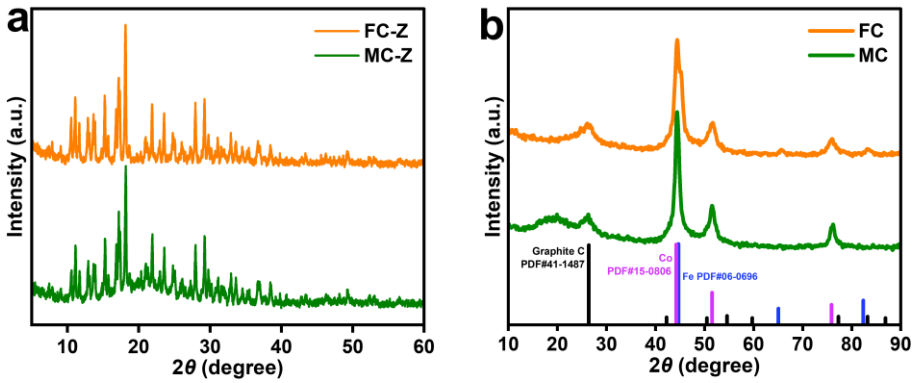

Fig. S11 XRD patterns of a) MC-Z and FC-Z, and b) MC and FC.

Compared to MC-Z, no new diffraction peaks appeared in FC-Z, implying that the introduction of Fe^{3+} hardly modified the crystal structure of the precursor. The color of the mixed solution changed from its original purple to lavender upon the addition of Fe^{3+}, and the reaction was significantly less intense than that of FZ-Z. Following pyrolysis, the metallic Co phase was visible in MC in addition to the graphitic carbon phase. The diffraction peaks were located at 44.3°, 51.5°, and 76.1°, corresponding to the (111), (200), and (220) crystal planes of metallic Co, respectively. In FC, not only were the new diffraction peaks of the reduced metallic Fe phase observed, but a significant reduction in the intensity of the diffraction peaks associated with metallic Co was also found. The (110), (200), and (211) crystal planes of metallic Fe were responsible for the diffraction peaks at 44.9°, 65.5°, and 83.0°, respectively.

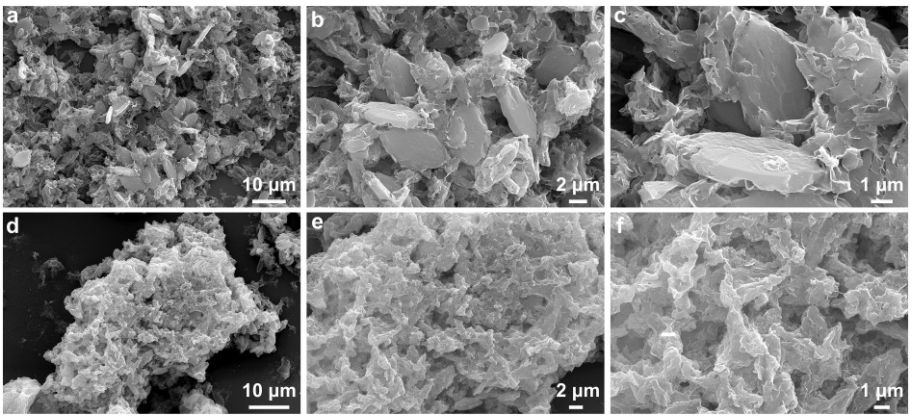

Fig. S12 SEM images of a-c) MC-Z and d-f) FC-Z.

The MC-Z precursor exhibited a leaf-like structure similar to that of CZ-Z, but with a rough surface. However, the structure transformed into a poorly outlined, stacked blocky structure after the introduction of Fe^{3+}.

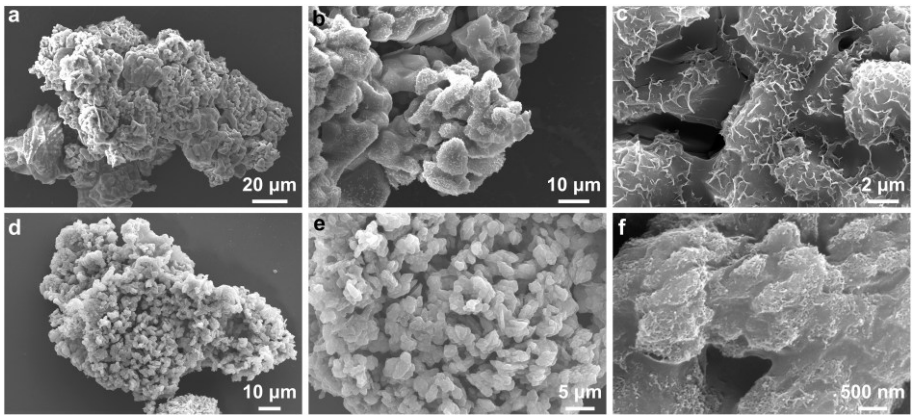

Fig. S13 SEM images of a-c) MC and d-f) FC.

The structure of MC also collapsed into stacked clusters, whereas the Fe^{3+}-introduced FC perfectly preserved the precursor structure, displaying an elongated block morphology.

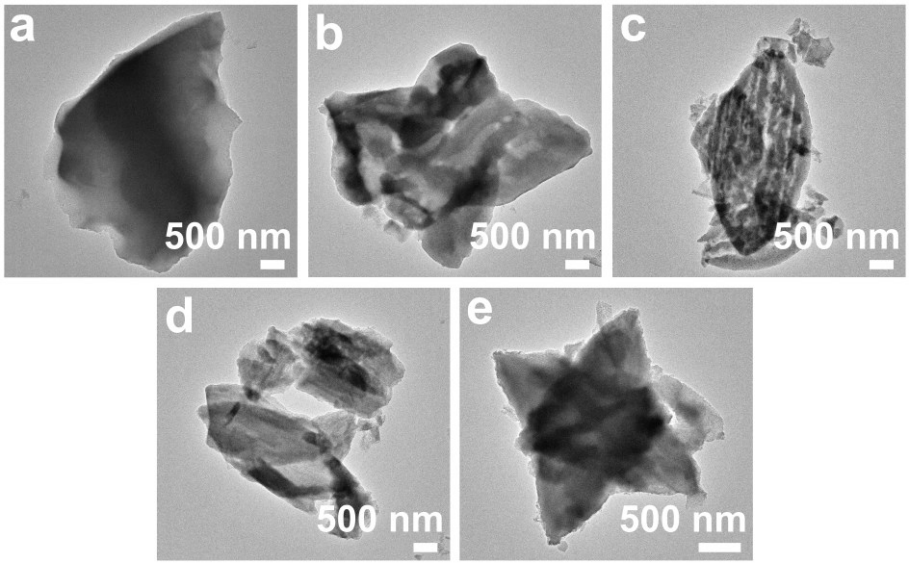

Fig. S14 TEM images of a) CZ, b) FCZ1, c) FCZ2, d) FCZ3, and e) FCZ5.

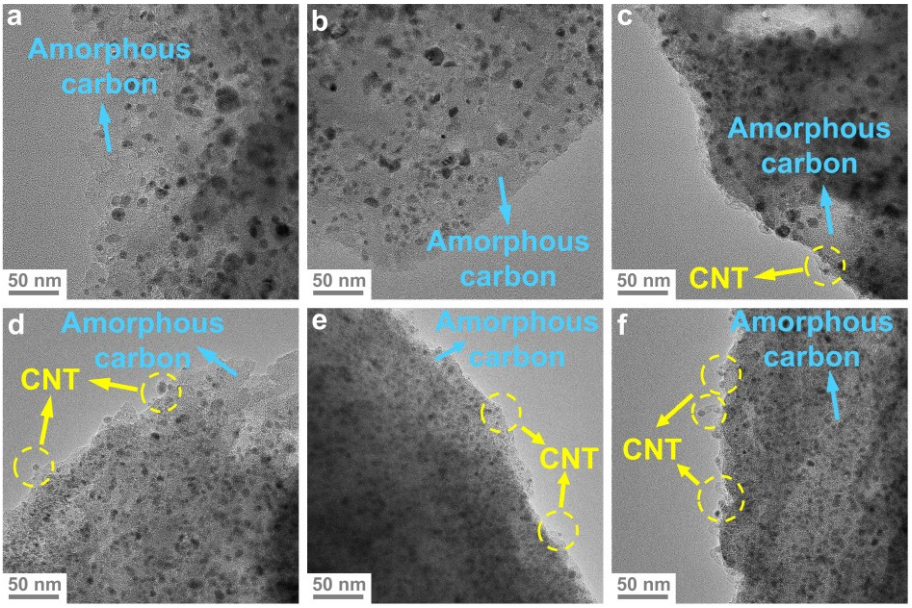

Fig. S15 TEM images of a) CZ, b) FCZ1, c) FCZ2, d) FCZ3, e) FCZ4, and f) FCZ5.

Metal NPs of various sizes, anchored to the amorphous carbon matrix, were observed in all samples. With the increase in Fe^{3+} concentration, the presence of carbon nanotubes (CNTs) was distinctly found at the edge of the carbon substrate, verifying the role of Fe-catalyzed carbon-directed growth at high temperatures.

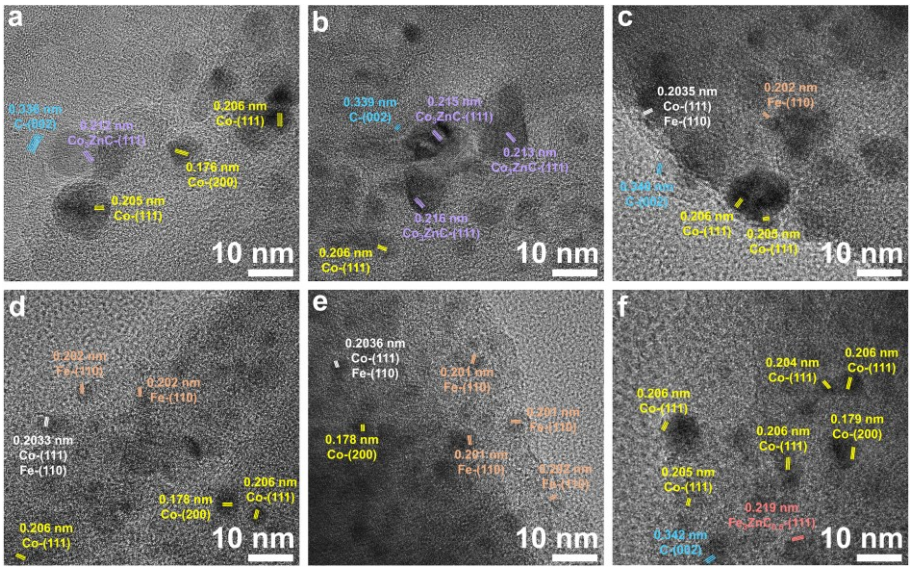

Fig. S16 HRTEM images of a) CZ, b) FCZ1, c) FCZ2, d) FCZ3, e) FCZ4, and f) FCZ5.

The HRTEM-derived lattice parameters are consistent with the XRD results. Notably, indistinguishable lattice spacing values intermediate between the metallic Fe and Co phases were identified in multiple samples following Fe^{3+} incorporation.

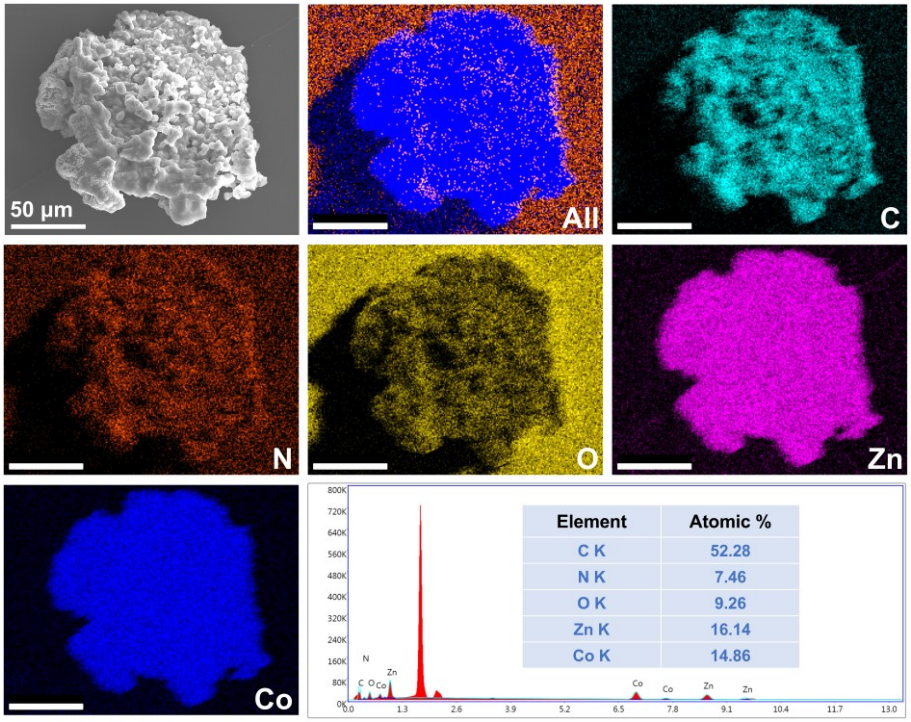

Fig. S17 SEM-EDS elemental mapping of CZ (all images were on a 50 μm scale bar).

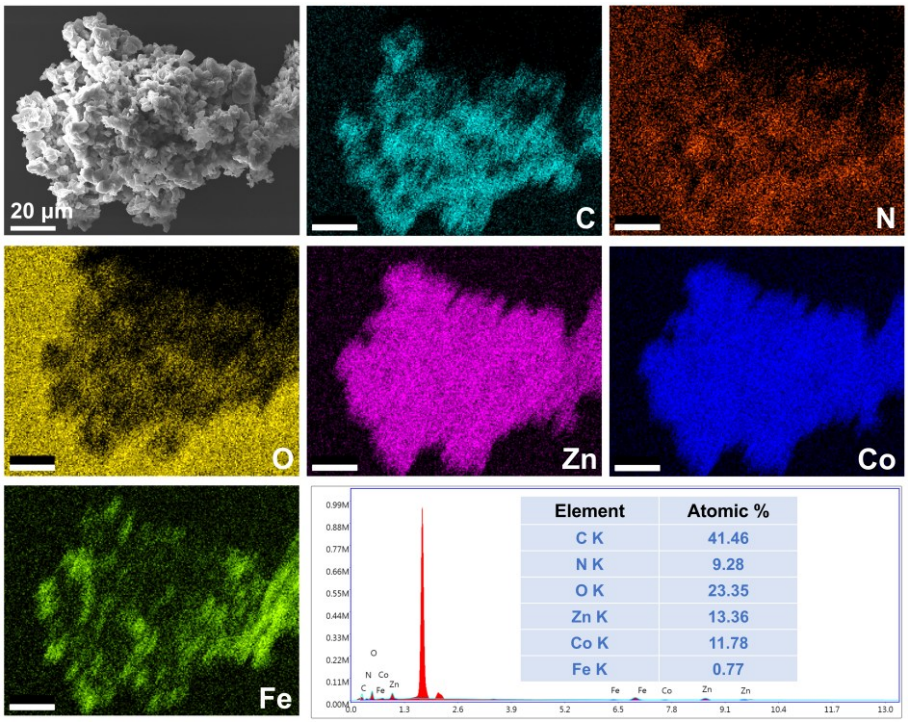

Fig. S18 SEM-EDS elemental mapping of FCZ1 (all images were on a 20 μm scale bar).

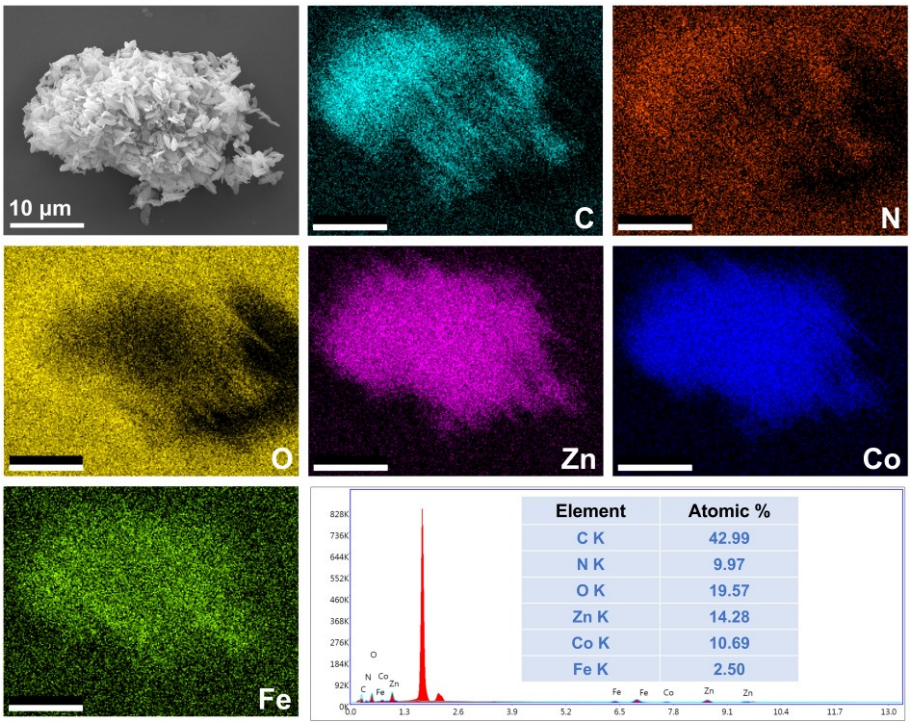

Fig. S19 SEM-EDS elemental mapping of FCZ2 (all images were on a 10 μm scale bar).

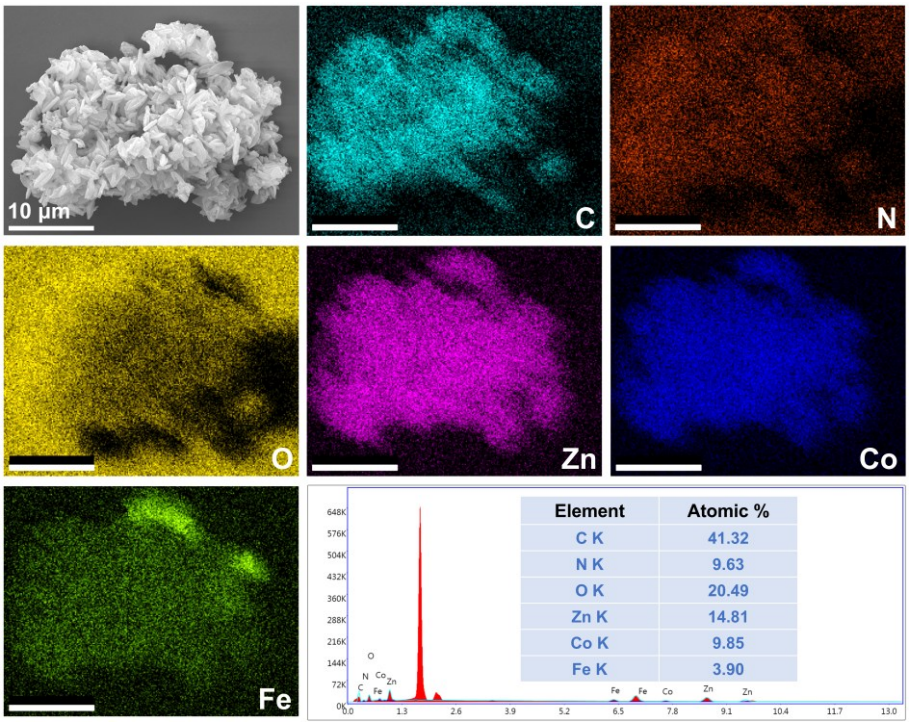

Fig. S20 SEM-EDS elemental mapping of FCZ3 (all images were on a 10 μm scale bar).

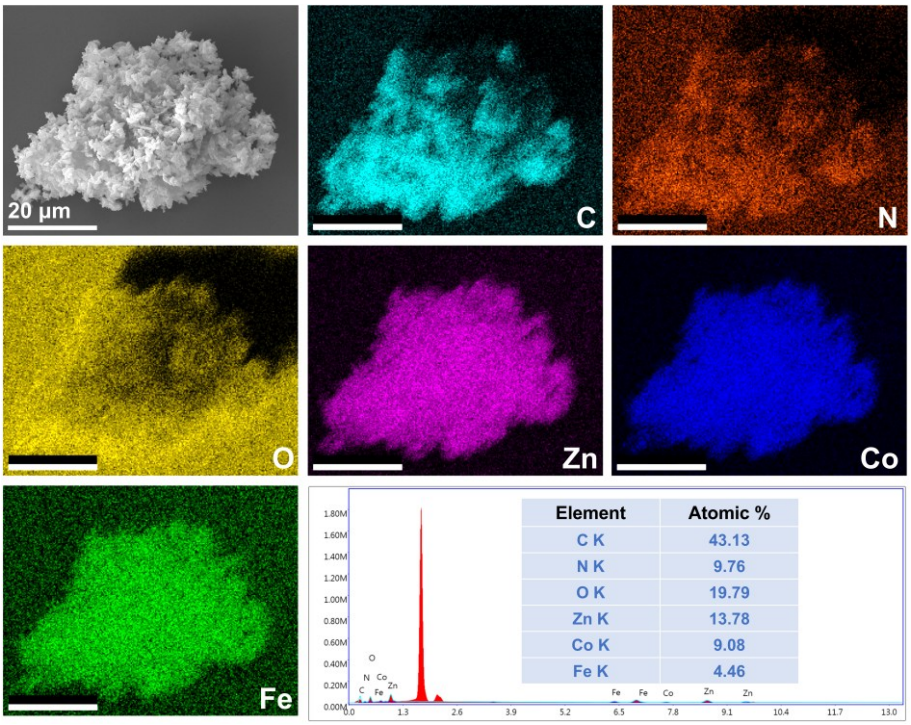

Fig. S21 SEM-EDS elemental mapping of FCZ4 (all images were on a 20 μm scale bar).

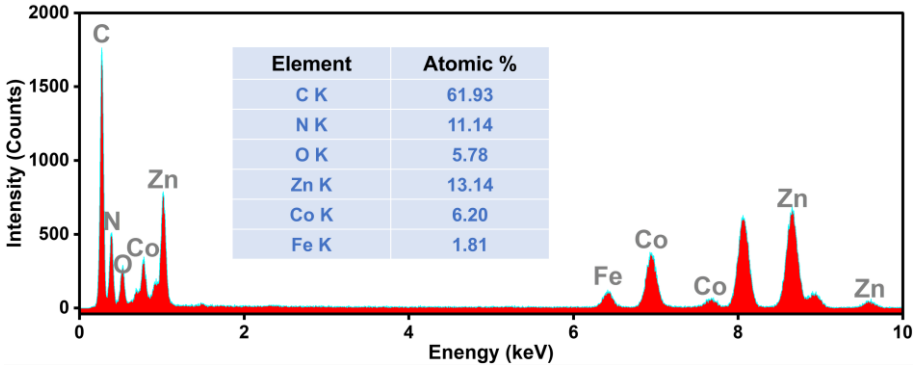

Fig. S22 TEM-EDS elemental mapping result of FCZ4.

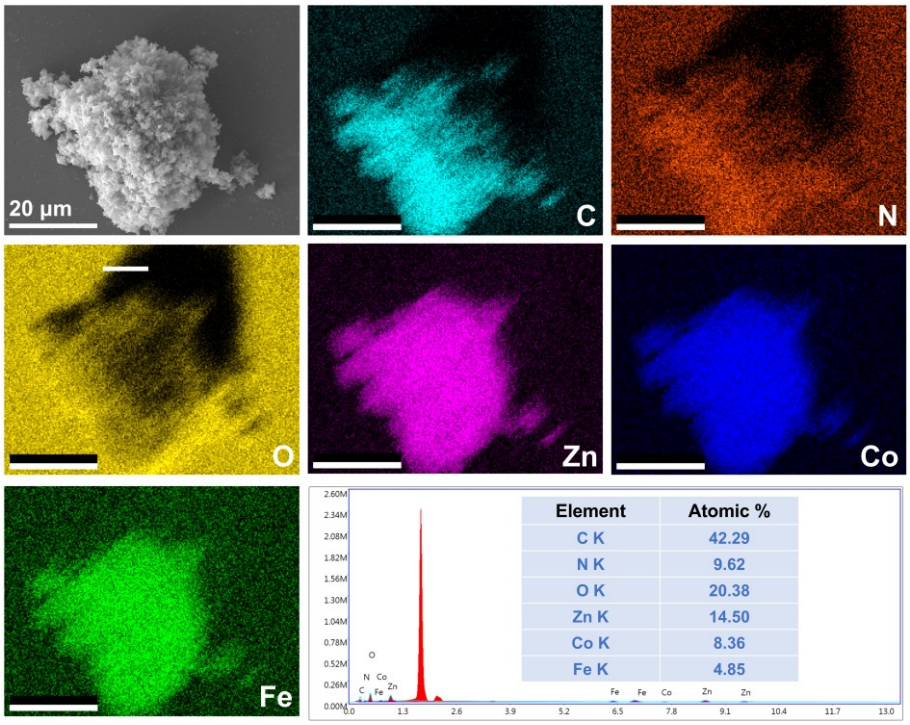

Fig. S23 SEM-EDS elemental mapping of FCZ5 (all images were on a 20 μm scale bar).

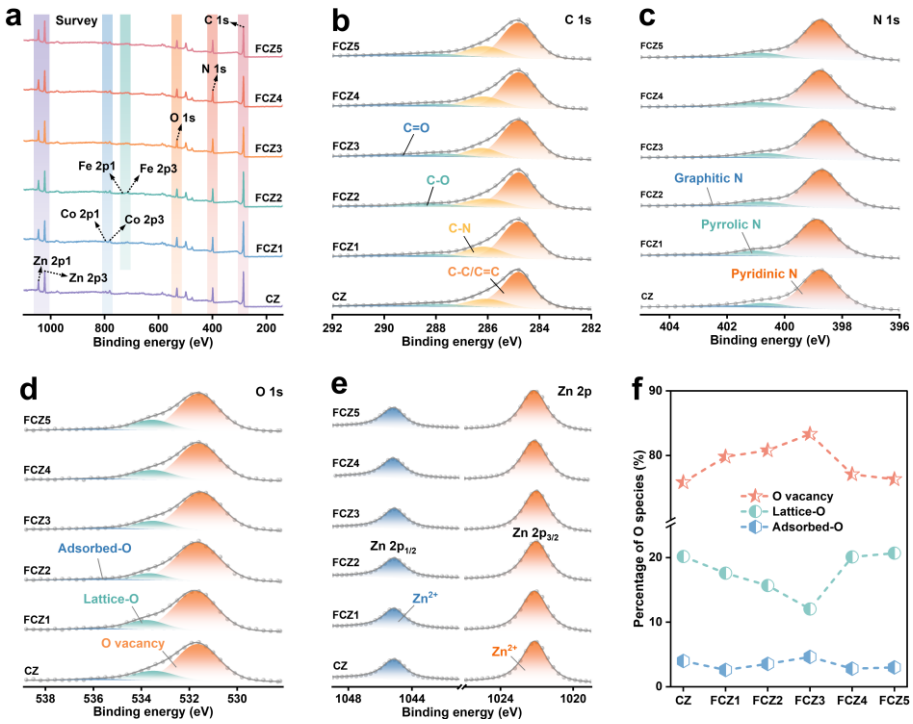

Fig. S24 a) XPS survey spectra, b) C 1s spectrum, c) N 1s spectrum, d) O 1s spectrum, and e) Zn 2p spectrum of CZ and FCZ*x*. f) Percentage of oxygen species.

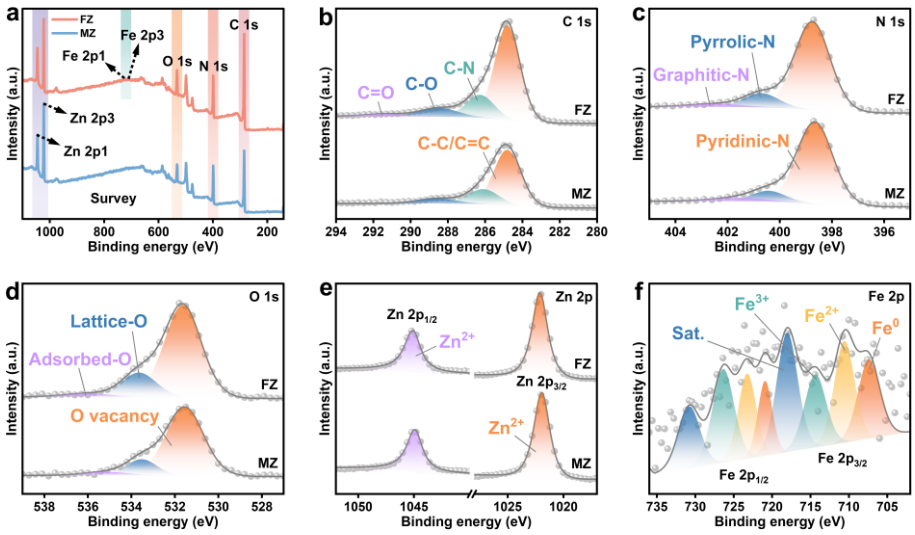

Fig. S25 a) XPS survey spectra, b) C 1s spectrum, c) N 1s spectrum, d) O 1s spectrum, and e) Zn 2p spectrum of MZ and FZ. f) Fe 2p spectrum of FZ.

The elemental distribution of C 1s, N 1s, and O 1s species in MZ exhibited compositional characteristics nearly identical to those observed in the bimetallic system. Notably, distinct characteristic peaks corresponding to Zn $2p_{1/2}$ and Zn $2p_{3/2}$ were identified in both MZ and FZ materials through XPS analysis. This observation, combined with the absence of Zn-related crystalline diffraction patterns in XRD characterization, strongly indicated the existence of Zn in the form of an amorphous ZnO phase dispersed within the carbon matrix. Observing Fe^0 species in the high-resolution Fe 2p spectrum of FZ supported the generation of metallic Fe and $Fe_3ZnC_{0.5}$ phases. High valence states of Fe^{2+} and Fe^{3+} were detected, potentially resulting from oxidation of the material surface.

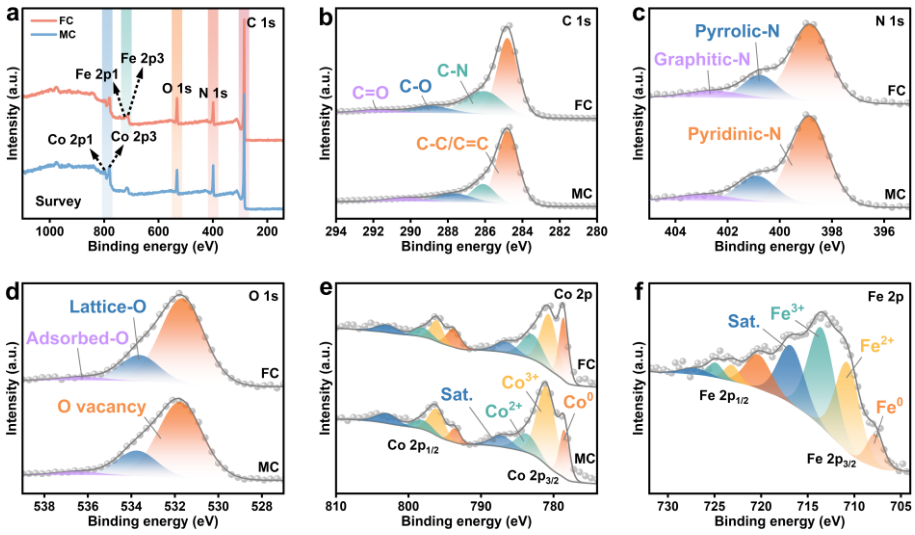

Fig. S26 a) XPS survey spectra, b) C 1s spectrum, c) N 1s spectrum, d) O 1s spectrum, and e) Co 2p spectrum of MC and FC. f) Fe 2p spectrum of FC.

The species detected in the high-resolution C 1s, N 1s, and O 1s spectra in MC were almost identical to those in the bimetallic system. The generation of metallic Co and metallic Fe was further corroborated by the detection of Co^0 and Fe^0 species in the high-resolution Co 2p and Fe 2p spectra, which agreed with the results of XRD. The observed high valence states of Co (Co^{2+}/Co^{3+}) and Fe (Fe^{2+}/Fe^{3+}) may be caused by the partial oxidation of the surface of the material exposed to air.

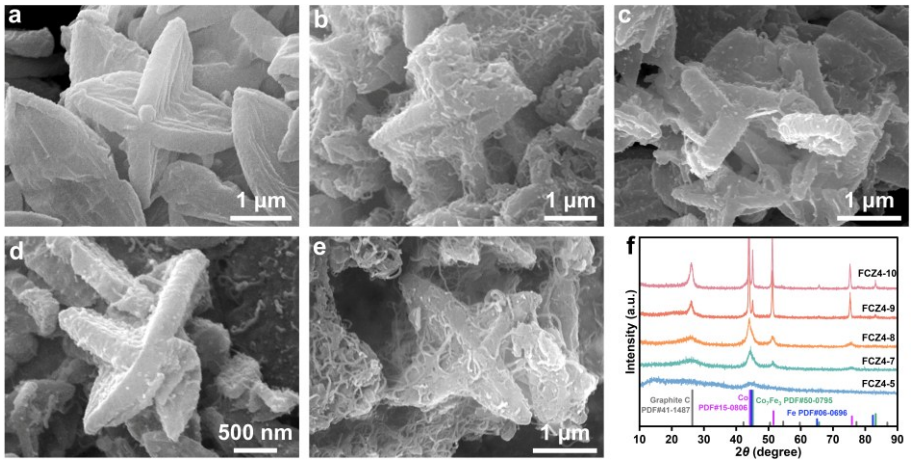

Fig. S27 SEM images of a) FCZ4-5, b) FCZ4-7, c) FCZ4-8, d) FCZ4-9, and e) FCZ4-10. f) XRD patterns of FCZ4-*y*.

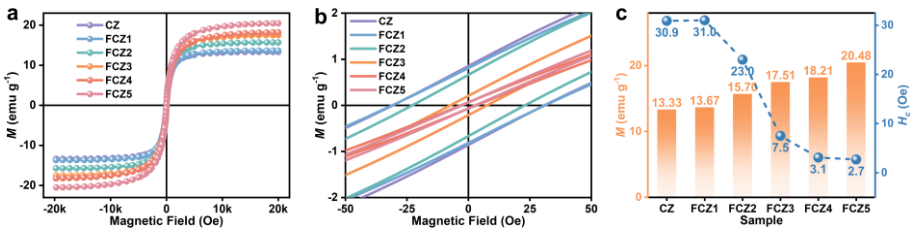

Fig. S28 Magnetization (*M*-*H*) curves measured at room temperature.

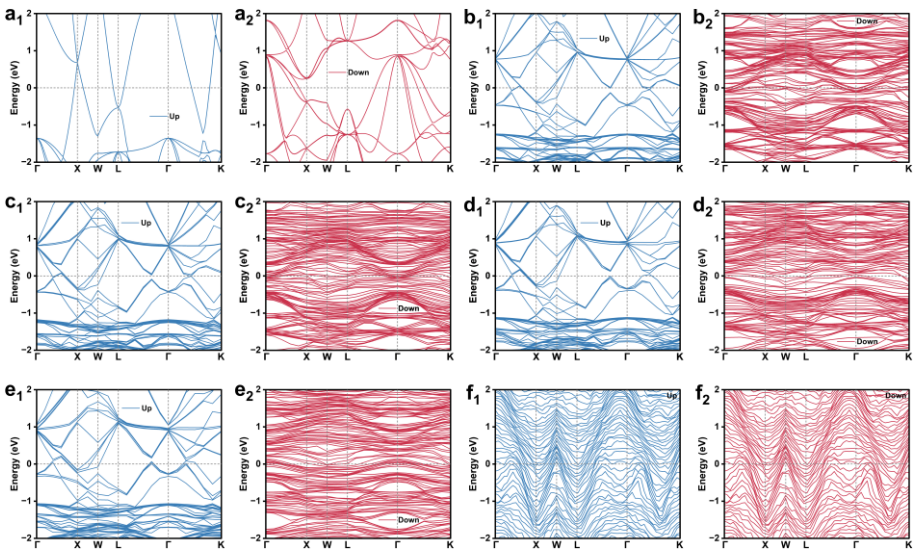

Fig. S29 The band structure after geometric optimization. Spin-up and spin-down of the band structure of a) Co (*Fm-3m*), b) Fe_2Co_{30}, c) Fe_4Co_{28}, d) Fe_8Co_{24}, e) $Fe_{12}Co_{20}$, and f) $Fe_{16}Co_{16}$.

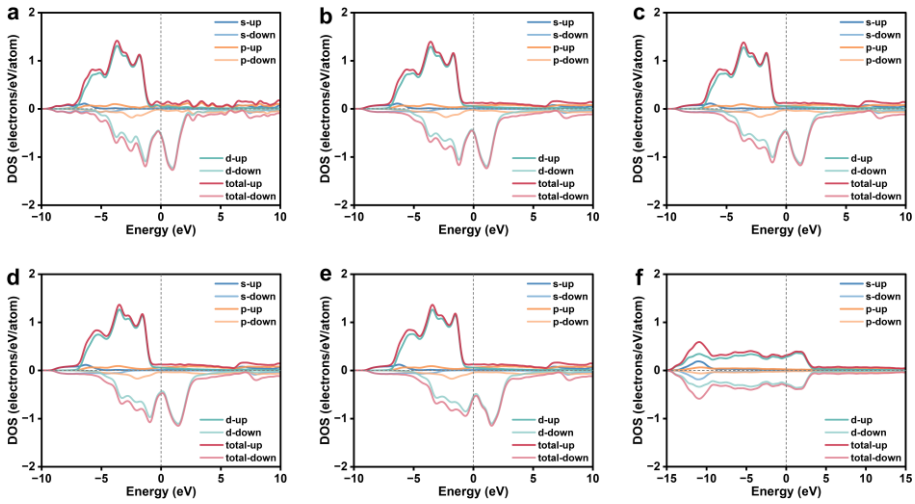

Fig. S30 The PDOS of a) Co, b) Fe_2Co_{30}, c) Fe_4Co_{28}, d) Fe_8Co_{24}, e) $Fe_{12}Co_{20}$, and f) $Fe_{16}Co_{16}$.

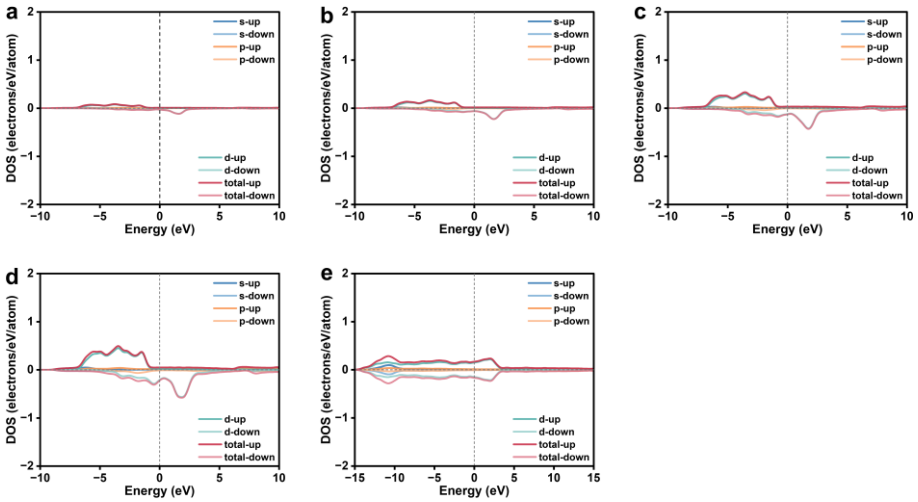

Fig. S31 The Fe-PDOS of a) Fe_2Co_{30}, b) Fe_4Co_{28}, c) Fe_8Co_{24}, d) $Fe_{12}Co_{20}$, and e) $Fe_{16}Co_{16}$.

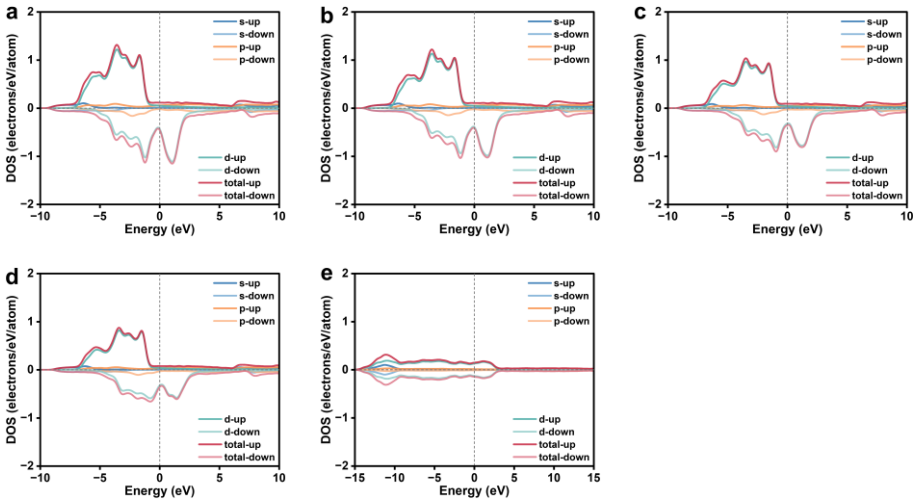

Fig. S32 The Co-PDOS of a) Fe_2Co_{30}, b) Fe_4Co_{28}, c) Fe_8Co_{24}, d) $Fe_{12}Co_{20}$, and e) $Fe_{16}Co_{16}$.

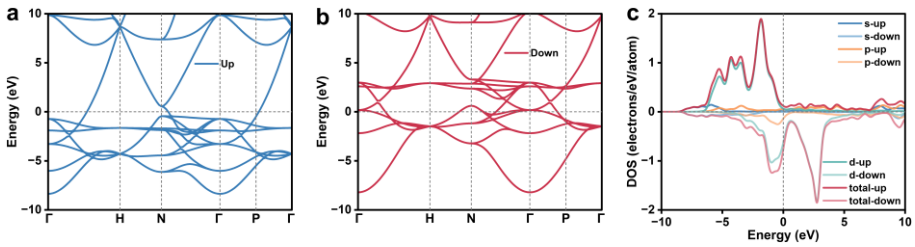

Fig. S33 The band structure and PDOS of Fe (*Im-3m*) after geometric optimization. a) Spin-up and b) spin-down of the band structure. c) PDOS.

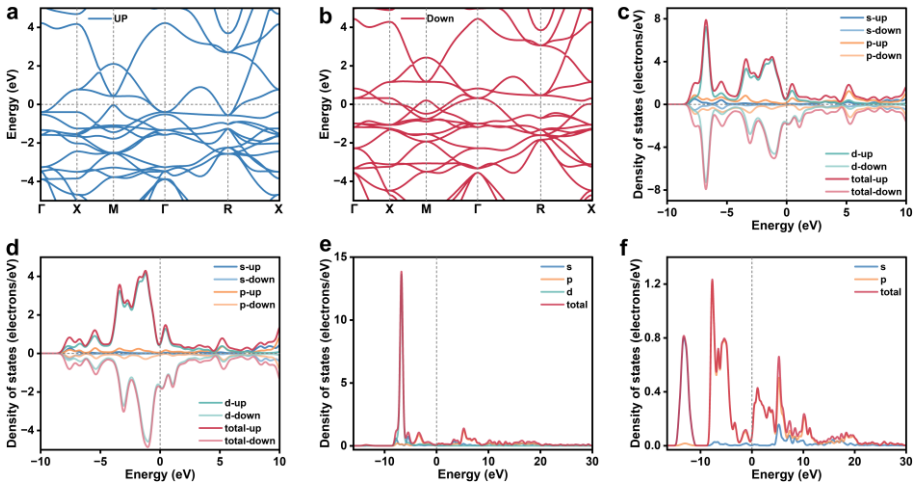

Fig. S34 The band structure and PDOS of Co_3ZnC after geometric optimization. a) Spin-up and b) spin-down of the band structure. c) All, d) Co, e) Zn, and f) C of PDOS.

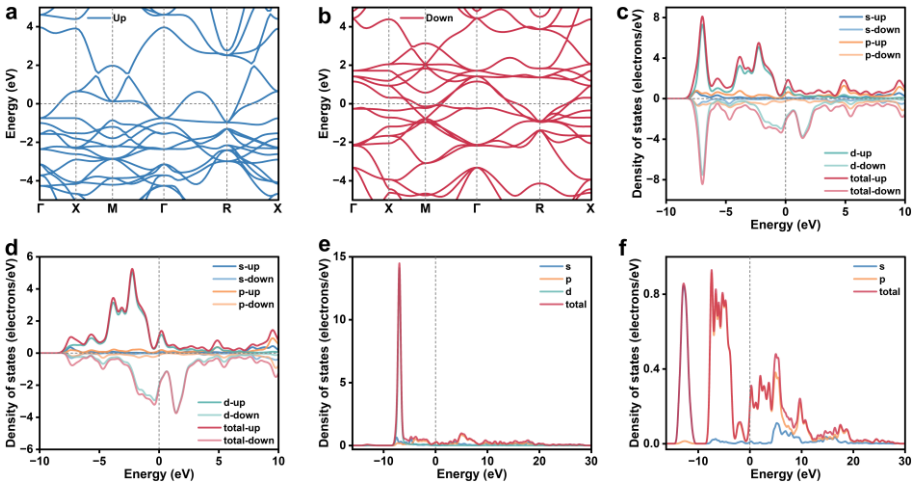

Fig. S35 The band structure and PDOS of $Fe_3ZnC_{0.5}$ after geometric optimization. a) Spin-up and b) spin-down of the band structure. c) All, d) Fe, e) Zn, and f) C of PDOS.

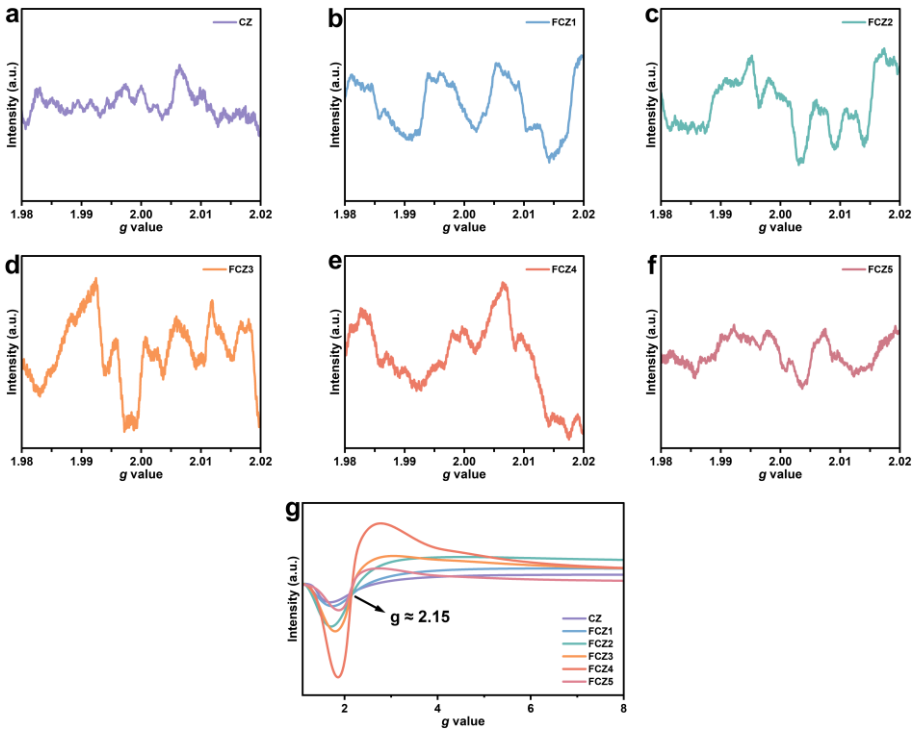

Fig. S36 EPR narrow spectrum signal of a) CZ, b) FCZ1, c) FCZ2, d) FCZ3, e) FCZ4, and f) FCZ5. g) EPR full-spectrum signal.

While the noisy peaks within narrow spectral ranges lacked sufficient resolution to identify the characteristics of unpaired electrons, systematic variations in integrated peak intensities demonstrated strong correlations with the evolving concentrations of paramagnetic centers and unpaired electron populations. The broad EPR signals centered at g ≈ 2.15 suggested the presence of paramagnetic centers, likely attributed to high-spin Fe^{3+} species or unpaired electrons in Fe-Co solid solutions. The intensity variation of signal peaks observed in the full spectrum exhibited identical behavior to that detected in the narrow spectrum, demonstrating that the Fe^{3+} species or Fe-Co solid solutions initially increased proportionally with Fe incorporation concentration. This enhancement peaked at 2.4 mmol Fe loading and subsequently displayed a declining trend.

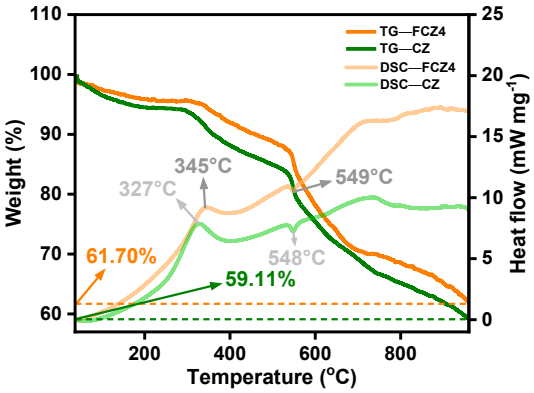

Fig. S37 The TG and DSC curves of CZ and FCZ4.

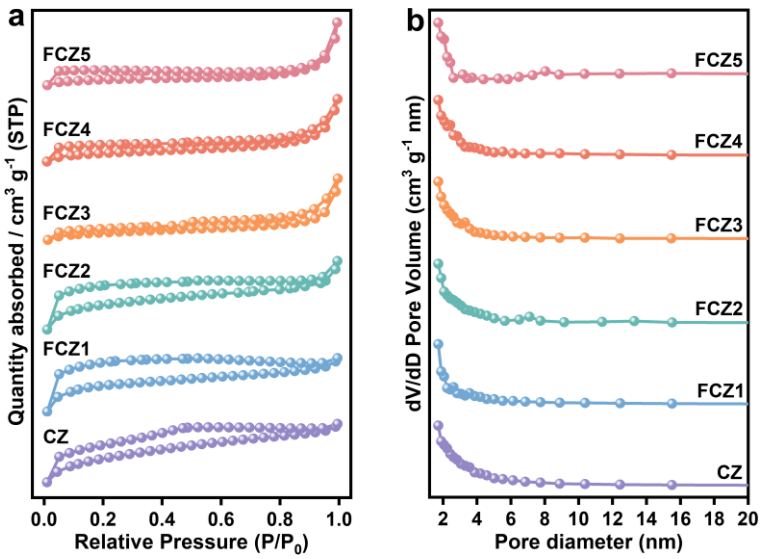

Fig. S38 a) N_2 adsorption-desorption isotherms. b) The pore size distribution curves.

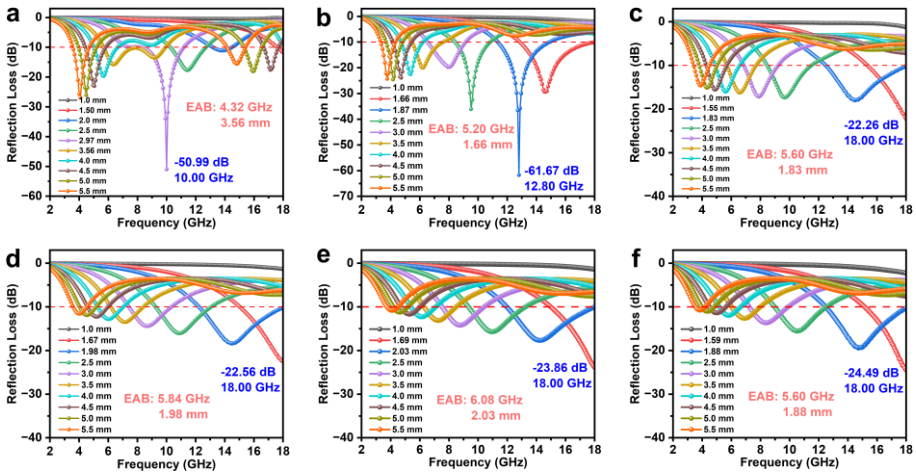

Fig. S39 The RL curves of a) CZ, b) FCZ1, c) FCZ2, d) FCZ3, e) FCZ4, and f) FCZ5 (at mass-filling ratios of 50%).

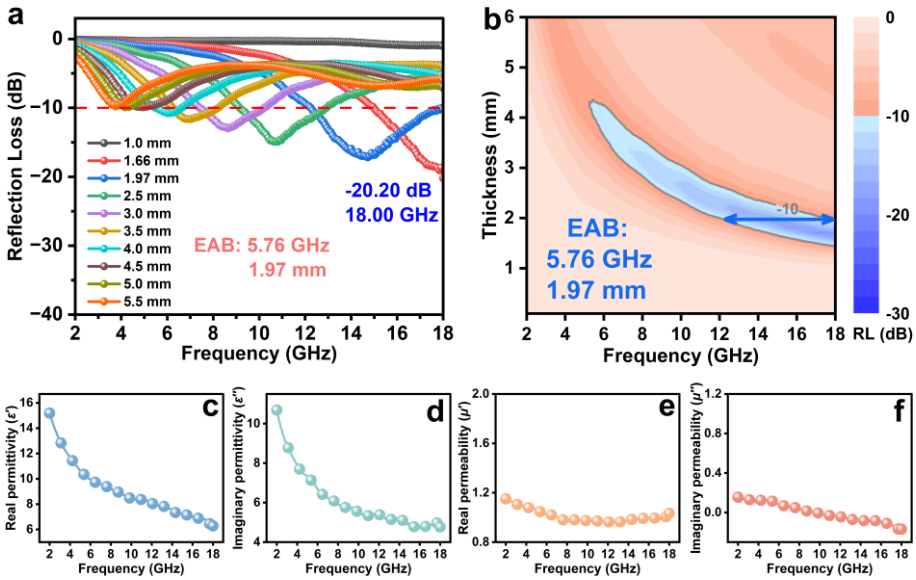

Fig. S40 a,b) The RL curves and 2D RL mapping of FCZ4. c-f) Electromagnetic parameters at mass-filling ratios of 50% (tested on Agilent E5071C, supplied by Scientific Compass from Hangzhou Research Interest Information Technology Co., Ltd).

The RL_{min} and EAB obtained from retesting were in good agreement with the previous results, and the electromagnetic parameters were essentially the same, confirming the reliability and repeatability of FCZ4 composites for real-world electromagnetic wave absorption applications.

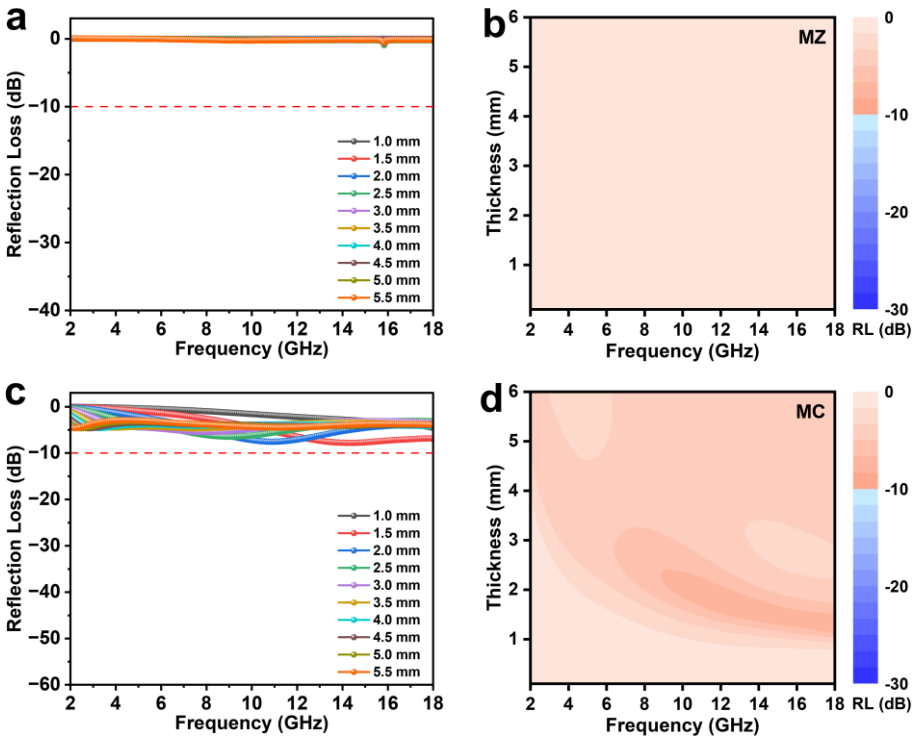

Fig. S41 The RL curves and 2D RL mapping of a,b) MZ and c,d) MC at mass-filling ratios of 50%.

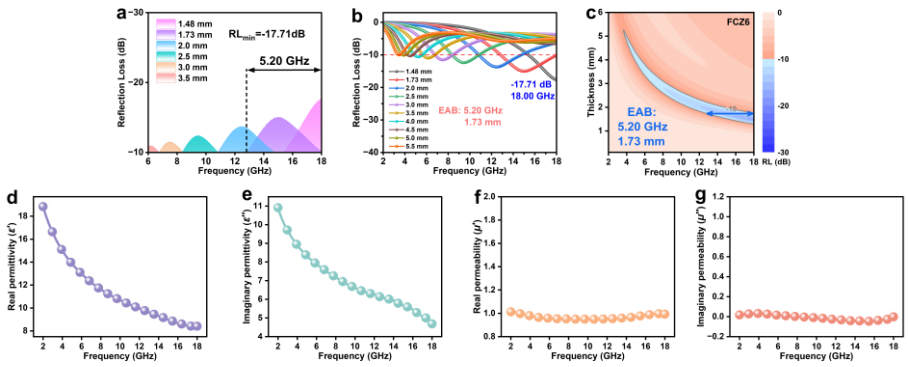

Fig. S42 a-c) The RL curves and 2D RL mapping of FCZ6. d-g) Electromagnetic parameters at mass-filling ratios of 50%.

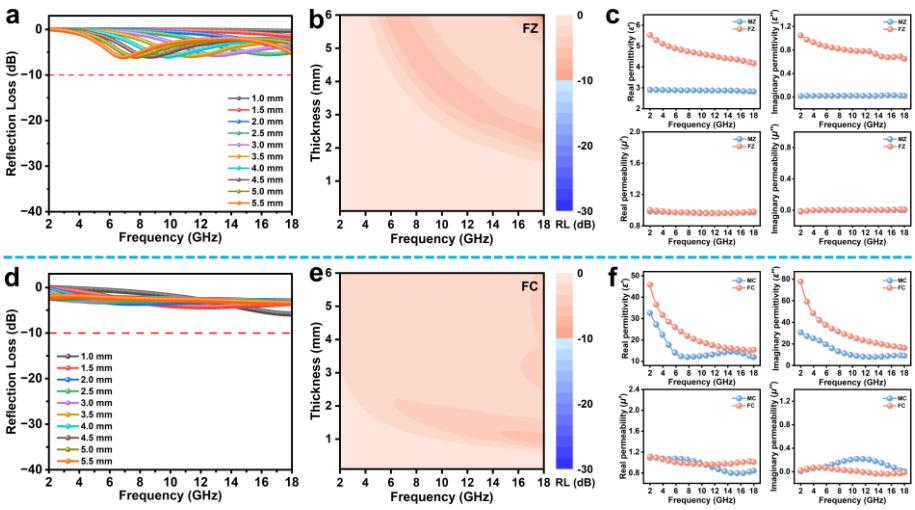

Fig. S43 The RL curves, 2D RL mapping, and electromagnetic parameters of a-c) FZ and d-f) FC at mass-filling ratios of 50%.

FZ displayed a remarkable improvement in performance over MZ. Although the properties of FC were comparable to those of MC, a significant strengthening of the dielectric response was observed. These results illustrated the effectiveness of introducing Fe^{3+} into bimetallic MOF systems in enhancing the dissipation capacity of electromagnetic waves.

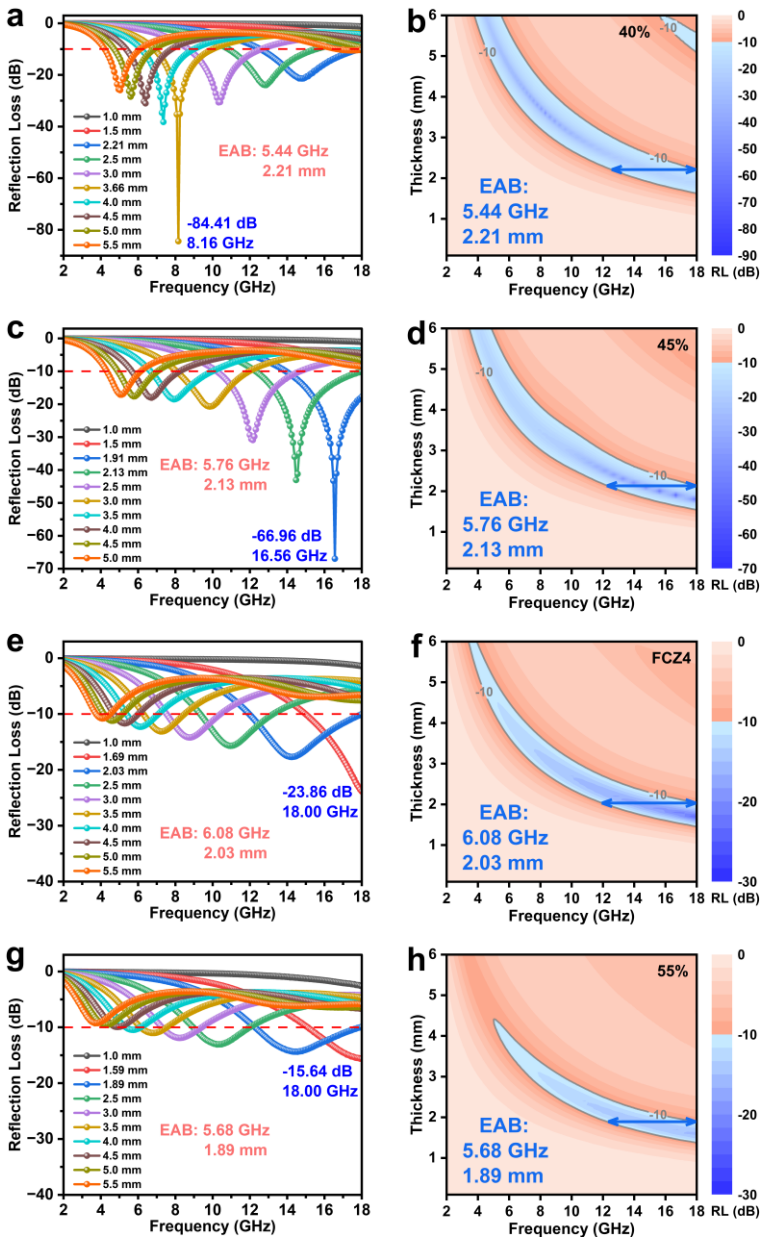

Fig. S44 The RL curves and 2D RL mapping of FCZ4 at different mass-filling ratios of a,b) 40%, c,d) 45%, e,f) 50%, and g,h) 55%.

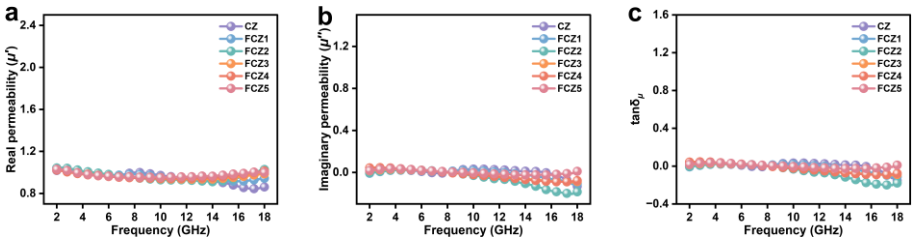

Fig. S45 a) The real part and b) the imaginary part of the complex permeability. c) The magnetic loss tangent values (at mass-filling ratios of 50%).

This may be due to the Fabry-Pérot resonance (FPR) effect that occurred in this high-loss material during testing [23]. This can lead to the appearance of counterfactual dielectric parameters. Due to the FPR effect, selecting an appropriate thickness was crucial to obtain accurate dielectric parameters based on the test method. For the single TE mode of the waveguide in the band, the wavelength can be expressed as [23, 24]:

$$\lambda g = 1/Re\left[\left(\frac{\varepsilon_r \mu_r f^2}{v_0^2} - \frac{1}{\lambda_c^2}\right)^{1/2}\right] \tag{21}$$

If the sample thickness was $\lambda_g/2$, the FPR will occur, which can manipulate the reflection of the electromagnetic field. For magnetic materials, the optimal thickness of the samples should be $\lambda_g/4$ at the minimum frequency in the investigated range. A smaller thickness would result in a much greater error, whereas a larger thickness would lead to a counterfactual result due to FPR. In contrast, the sample exhibited higher electromagnetic parameters, resulting in stronger losses, and the FPR errors that occurred are larger. In addition, the inhomogeneity of the sample dimensions can also lead to the appearance of such problems.

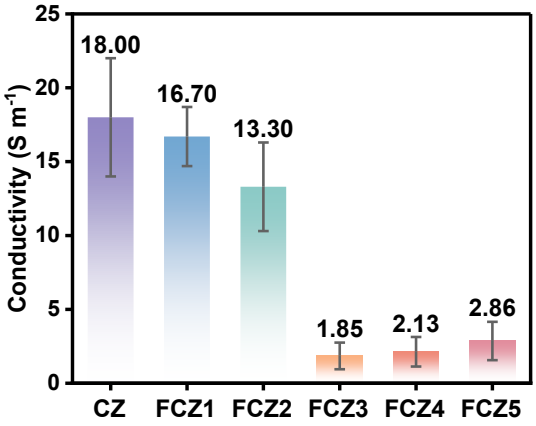

Fig. S46 Electrical conductivity on samples with 100 wt% filler loading measured by a four-point probe.

The electrical conductivity of pristine samples displayed a characteristic non-monotonic variation with increasing Fe^{3+} incorporation concentration, exhibiting a minimum at FCZ3 while paralleling the conductivity evolution observed in 50 wt% paraffin-containing composites. Although the intrinsic conductivity values of the samples reflected their inherent material properties, the electromagnetic parameters were obtained from composite paraffin-based measurements. Thus, the reported conductivity data here primarily served as an indicator for analyzing variation trends.

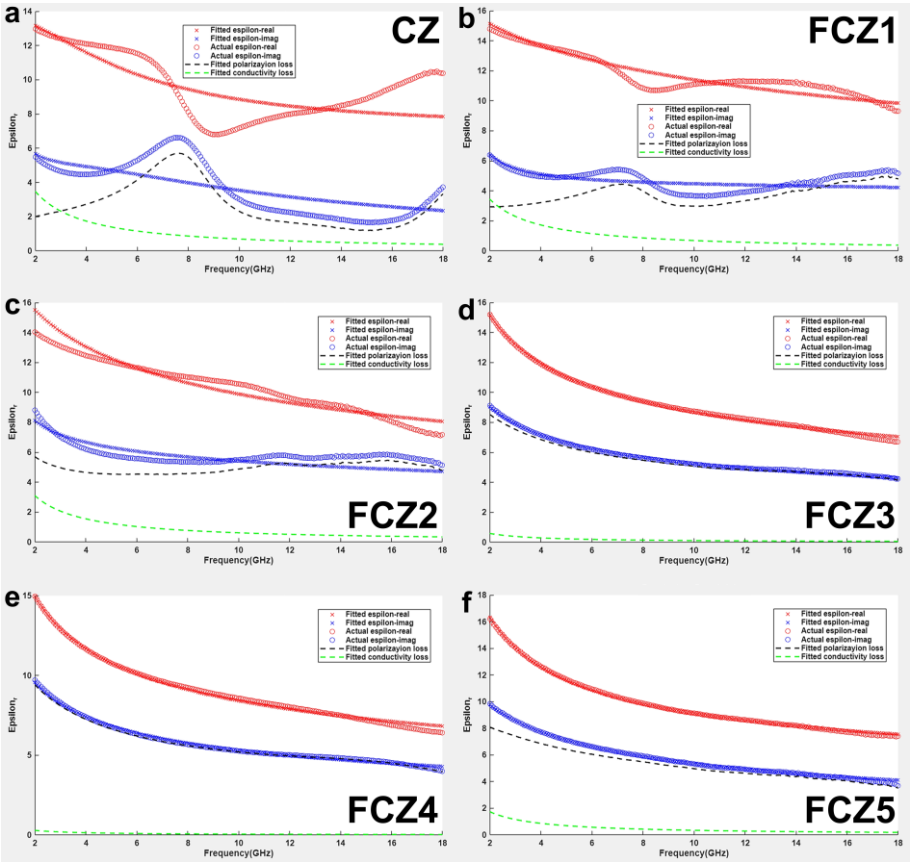

Fig. S47 Fitting curves using the modified Havriliak-Negami model of a) CZ, b) FCZ1, c) FCZ2, d) FCZ3, e) FCZ4, and f) FCZ5.

The real and imaginary parts of the complex permittivity derived from the fitting exhibited a good overlap with the experimentally measured data, while the fitted conductivity loss and polarization loss closely aligned with the corresponding experimental values. Collectively, this validated the accuracy and reliability of the theoretical model employed to describe the electromagnetic response characteristics of the material systems.

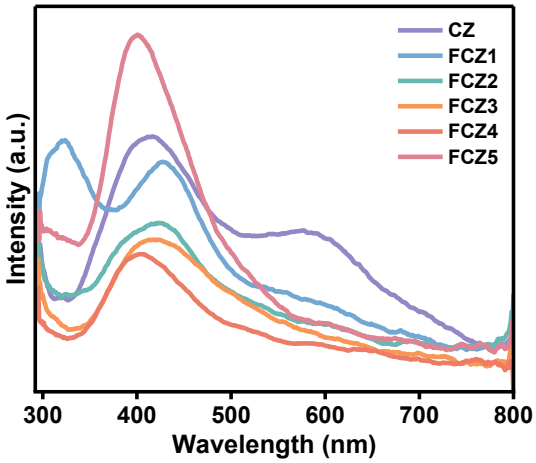

Fig. S48 PL spectrogram of different samples.

The PL analysis revealed that the absorption peaks in the 350-450 nm spectral range exhibited an increasing and then decreasing trend with elevating Fe^{3+} introduction concentration, with the FCZ4 sample displaying the minimum intensity. This phenomenon suggested that the intrinsic defect density underwent progressive enhancement with Fe^{3+} incorporation, attaining maximum values at the FCZ4 before subsequent reduction at higher incorporation levels.

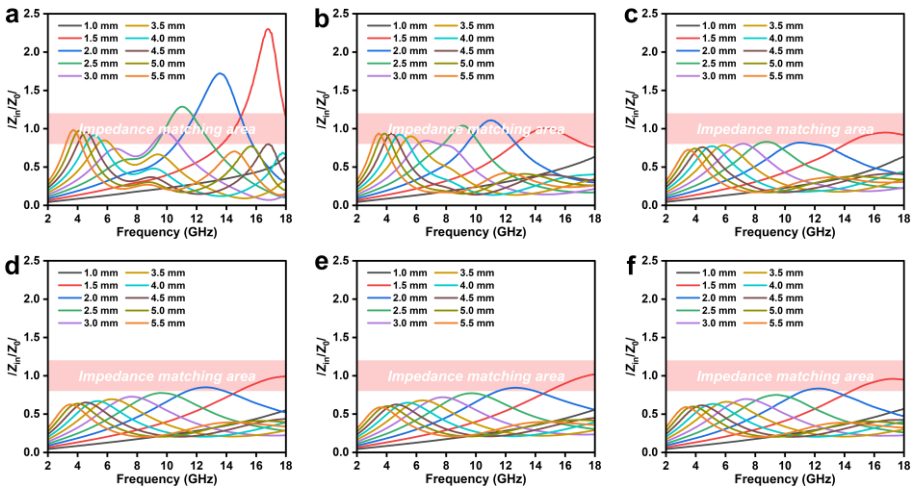

Fig. S49 The impedance matching of a) CZ, b) FCZ1, c) FCZ2, d) FCZ3, e) FCZ4, and f) FCZ5 (at mass-filling ratios of 50%).

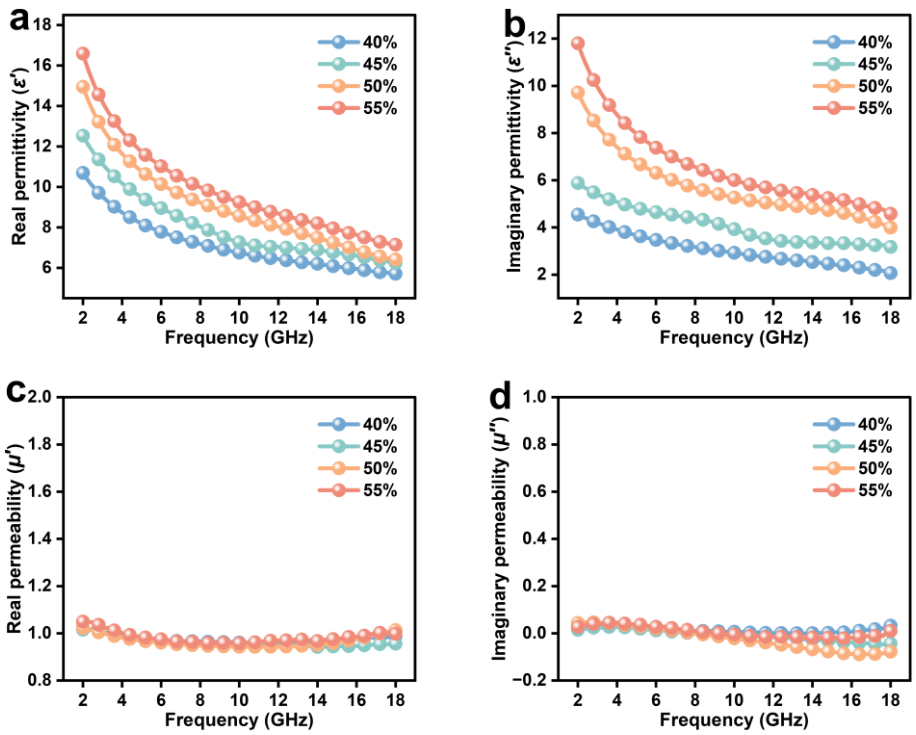

Fig. S50 a) The real part and b) the imaginary part of the complex permittivity of FCZ4 at different mass-filling ratios. c) The real part and d) the imaginary part of the complex permeability of FCZ4 at different mass-filling ratios.

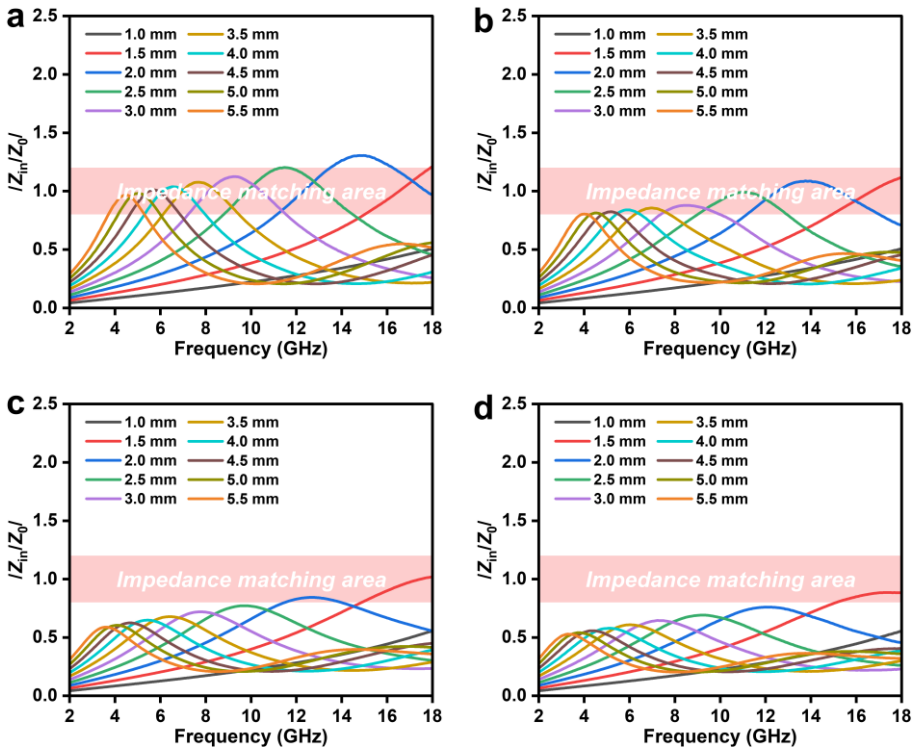

Fig. S51 The impedance matching of FCZ4 at different mass-filling ratios of a) 40%, b) 45%, c) 50%, and d) 55%.

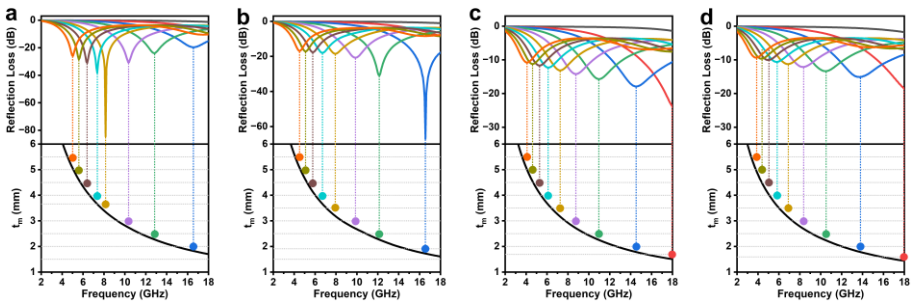

Fig. S52 Dependence of λ/4 matching thickness on RL peaks for FCZ4 at different mass-filling ratios of a) 40%, b) 45%, c) 50%, and d) 55%.

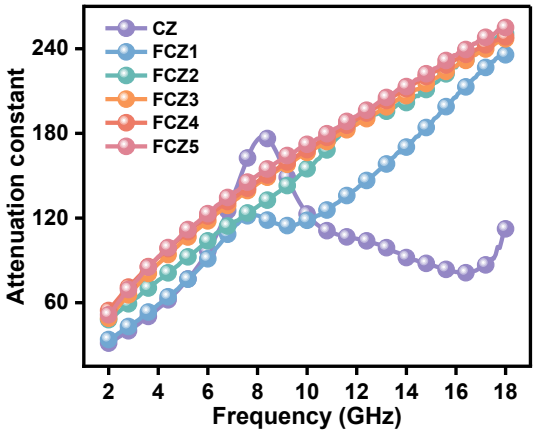

Fig. S53 The attenuation constant of different samples (at mass-filling ratios of 50%).

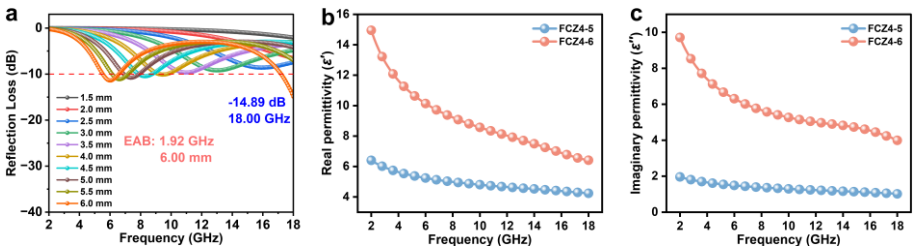

Fig. S54 a) The RL curves of FCZ4-5. b) The real part and c) the imaginary part of the complex permittivity of FCZ4-5 and FCZ4-6 (at mass-filling ratios of 50%).

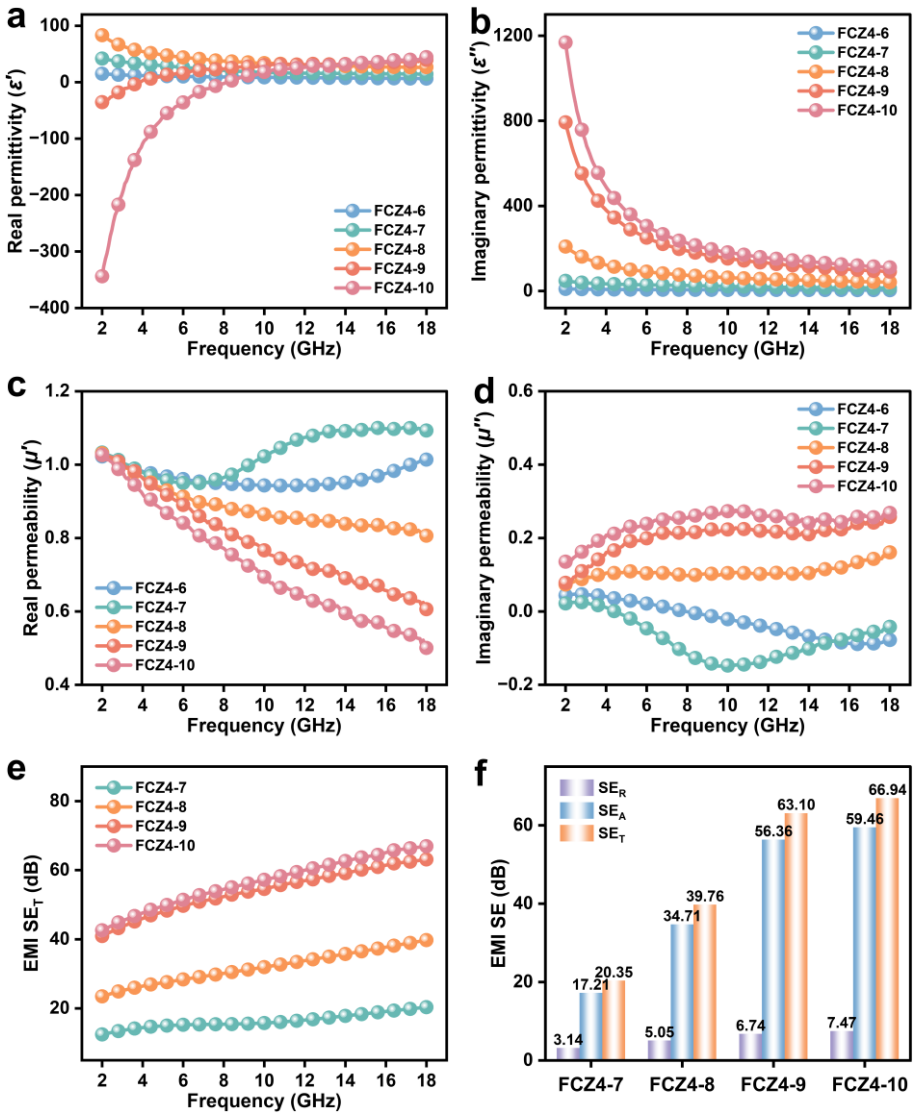

Fig. S55 Electromagnetic shielding properties of samples obtained at different heat treatment temperatures at mass-filling ratios of 50%. a) The real part and b) the imaginary part of the complex permittivity. c) The real part and d) the imaginary part of the complex permeability. e) EMI SE_T curves, and f) a summary of maximum EMI SE_T, SE_A, and SE_R values of FCZ4-*y*.

Electromagnetic shielding parameters were also obtained through coaxial method testing, which outputs both complex permittivity and permeability, as well as S-parameters, in a single measurement. All samples were filled with 50 wt% paraffin wax and had a thickness of 2.70 mm.

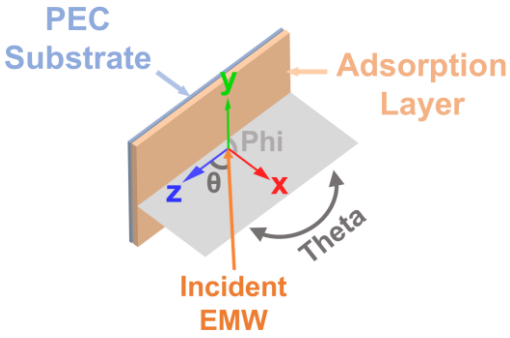

Fig. S56 Radar cross section simulation model.

The flat plate models (with a total size of 180 × 180 × 3.03 mm^3) included absorbers (180 × 180 × 2.03 mm^3) as the absorption layer and perfect electric conductor (PEC, 180 × 180 × 1.0 mm^3) as the reflection layer. The model was placed in the Y-O-Z plane with EMW incident from the Z-axis direction. Keeping the polarization angle φ constant while varying the incident angle θ (0°-180°) of the EMW. Here, 0° indicated a direction parallel to the Z-axis, while 90° denoted a direction parallel to the X-axis. At this angle (90°), the incident direction of the EMW was perpendicular to the model.

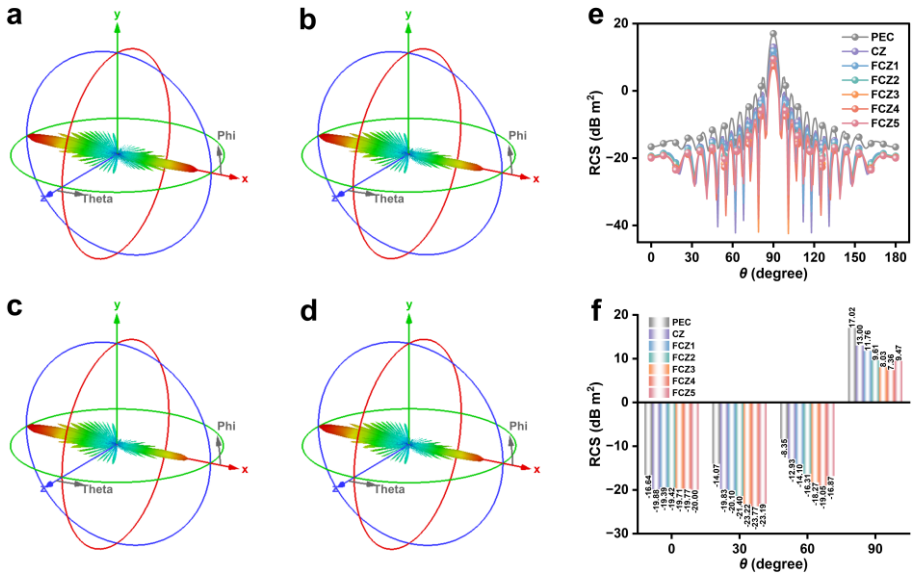

Fig. S57 3D radar scattering signal of a) FCZ1, b) FCZ2, c) FCZ3, and d) FCZ5. e) RCS simulation curves of different samples. f) RCS values under certain detection angles.

The RCS values of all the samples were found to be greater than those of the PEC, where the signal could be reduced by 3.36 dB m^2 at 0°, 9.70 dB m^2 at 30°, 10.70 dB m^2 at 60°, and 9.66 dB m^2 at 90°. This demonstrated that the as-synthesized composites were well-adapted to the outfield environment and held significant potential for practical applications.

Table S1 Sample name correspondence table

Sample name	$Zn(OAc)_2 \cdot 2H_2O$ (mmol)	$Co(NO_3)_2 \cdot 6H_2O$ (mmol)	$Fe(acac)_3$ (mmol)	2-Methylimidazole (mmol)	Heating temperature (°C)
MZ	24	/	/	100	600
FZ	24	/	2.4	100	600
MC	/	24	/	100	600
FC	/	24	2.4	100	600
CZ	12	12	/	100	600
FCZ1	12	12	0.6	100	600
FCZ2	12	12	1.2	100	600
FCZ3	12	12	1.8	100	600
FCZ4	12	12	2.4	100	600
FCZ5	12	12	3.0	100	600
FCZ6	12	12	3.6	100	600
FCZ4-5	12	12	2.4	100	500
FCZ4-6	12	12	2.4	100	600
FCZ4-7	12	12	2.4	100	700
FCZ4-8	12	12	2.4	100	800
FCZ4-9	12	12	2.4	100	900
FCZ4-10	12	12	2.4	100	1000

Remark:

(1) The precursors of all samples were denoted as "name-Z" (e.g., MZ-Z, CZ-Z, and FCZ-Z*x*).

(2) FCZ4 and FCZ4-6 represented the same sample.

Table S2 Mass content of the Zn, Co, and Fe elements obtained from ICP tests

Samples	Zn (wt%)	Co (wt%)	Fe (wt%)
CZ	17.36±0.02	13.56±0.04	/
FCZ1	14.73±0.01	10.43±0.09	0.42±0.01
FCZ2	15.21±0.01	10.09±0.02	1.49±0.01
FCZ3	14.80±0.03	9.33±0.03	1.83±0.01
FCZ4	15.51±0.04	9.56±0.10	2.76±0.01
FCZ5	16.00±0.02	9.46±0.02	3.27±0.03

Table S3 Atomic content of C, N, O, Zn, Co, and Fe elements calculated by XPS

Samples	C (at%)	N (at%)	O (at%)	Zn (at%)	Co (at%)	Fe (at%)
MZ	60.43	23.12	8.48	7.97	/	/
FZ	67.32	17.96	8.19	5.69	/	0.84
MC	74.68	13.65	8.77	/	2.90	/
FC	76.69	11.08	8.42	/	2.30	1.51
CZ	67.78	17.34	9.21	4.33	1.34	/
FCZ1	67.03	17.36	8.84	4.42	1.54	0.82
FCZ2	68.42	16.57	8.53	4.11	1.35	1.02
FCZ3	64.69	18.79	9.44	4.80	1.19	1.09
FCZ4	66.35	17.77	8.66	4.76	1.31	1.16
FCZ5	66.66	17.18	8.51	5.20	1.24	1.20

Table S4 Saturation magnetization (M_s) and coercivity (H_c) obtained from the *M-H* curves

Samples	Saturation magnetization (emu g^{-1})	Coercivity (Oe)
CZ	13.33	30.9
FCZ1	13.67	31.0
FCZ2	15.70	23.0
FCZ3	17.51	7.5
FCZ4	18.21	3.1
FCZ5	20.48	2.7

Table S5 Summary of per-atom and per-formula-unit formation energy after normalization of different models

Models	Per-atom formation energy (eV $atom^{-1}$)	Per-formula-unit formation energy (eV formula $unit^{-1}$)
C	-157.759388243325	-157.759388243325
Zn	-1,787.298703868000	-1,787.298703868000
Fe	-861.171167706500	-861.171167706500
Co	-1,098.193383181750	-1,098.193383181750
Fe_2Co_{30}	-103.708551013375	-207.417102026750
Fe_4Co_{28}	-88.899645151500	-177.799290303000
Fe_8Co_{24}	-59.282141467125	-118.564282934250
$Fe_{12}Co_{20}$	-29.527519425875	-59.055038851750
$Fe_{16}Co_{16}$	518.314675273188	1,036.629350546375
Co_3ZnC	0.054889947915	0.274449739575
$Fe_3ZnC_{0.5}$	0.127027761165	0.635138805825

Table S6 The comprehensive electromagnetic wave absorption performance comparison between FCZ4 and other previously reported MOF-based absorbers

Samples	RL_{min} (dB)	EAB (GHz)	Thickness (mm)	Loading (wt%)	Ref.
$CoSe_2$@N-C	−42.30	4.25	1.50	40	[1]
CoNiZn@Ti_3CNT_x@CF	−44.51	4.32	1.50	15	[2]
MoC/NC	−47.56	4.40	2.50	15	[3]
CoM@CoNiC-F	−64.78	4.60	2.30	/	[4]
Zn/NC	−50.50	5.10	1.90	20	[5]
CeO_2/Co/C	−71.50	5.20	1.60	40	[6]
$CoSe_2$@C	−40.10	5.20	2.00	30	[7]
FeCo@C	−50.57	5.35	1.80	28	[8]
Fe/Fe_3Co_7/Co/C	−64.70	5.80	2.50	40	[9]
Cu_9S_5/C	−69.60	5.81	1.83	20	[10]
CoFe/C	−70.80	6.00	2.30	2.2	[11]
$Fe(PO_3)_2$@C/PCF	−57.00	6.00	1.80	15	[12]
rGO/MD@CNTs	−51.60	5.90	2.00	6	[13]
MXene/CoNi@C	−38.40	5.80	1.50	30	[14]
Co@HNCSs	−65.40	5.40	1.60	30	[15]
MXene/CoFe@C/CNF	−63.90	5.20	1.90	3.4	[16]
Ni/C@rGO	−22.70	5.20	1.50	15	[17]
MIL-88A@NiFe @$Ti_3C_2T_x$	−46.70	5.12	1.80	/	[18]
C@Co/CIF	−45.65	4.80	1.35	30	[19]
CoNiZnO@NC	−70.70	4.48	1.55	30	[20]
Co/Ni-CNFs	−40.13	4.40	1.60	20	[21]
Ni@CNTs	−44.40	4.30	1.50	30	[22]
FCZ4	−88.41	5.44	2.21	40	This work
FCZ4	−66.96	5.76	2.13	45	This work
FCZ4	−23.86	6.08	2.03	50	This work

Table S7 Detailed fitting parameters using the modified Havriliak-Negami model

Samples	ε_s	ε_∞	τ	α	β	σ
CZ	15.2752	7.6447	0.0327	1.0000	1.0000	0.6145
FCZ1	13.4043	3.2283	0.0094	0.9445	1.0000	0.4816
FCZ2	16.9277	0	0.0450	0.6548	1.0000	0.3032
FCZ3	28.3320	4.3519	0.2275	0.5697	0.8455	0.1307
FCZ4	70.6510	0	3.9981	0.4367	0.7341	0.1226
FCZ5	89.5869	0	7.3359	0.4947	1.0000	0.2388

Note S1 Analysis of phase compositions in the CZ

Three phases of amorphous carbon, metallic Co, and Co_3ZnC intermetallic compounds were observed in the XRD pattern of CZ. Firstly, both amorphous carbon and metallic Co were synthesized by reduction during pyrolysis. The formation of the Co_3ZnC phase could be primarily ascribed to two key factors: i) The Co^{2+} (Co^{2+}/Co^0 = -0.277 V) exhibited a higher reduction potential compared to Zn^{2+} (Zn^{2+}/Zn^0 = -0.762 V), leading to its preferential reduction during the heat treatment process. This initial reduction stage consumed substantial reducing agents and diminished the reducing atmosphere, effectively suppressing subsequent Zn reduction. Under these constrained reduction conditions, the alloying behavior between Zn and Co demonstrated greater thermodynamic favorability than pure Zn reduction. ii) The significant atomic radius difference between Zn (0.139 nm) and Co (0.125 nm) established substantial lattice distortion energy barriers, which significantly impeded solid solution formation. Moreover, the absence of detectable diffraction peaks corresponding to Zn species was mainly due to the incomplete reduction of Zn during synthesis. This incomplete reduction process facilitated the dispersion of the material in an amorphous state or as ultrafine metallic particles across an amorphous carbon matrix, rendering it undetectable by conventional XRD techniques. Complementary XPS analysis confirmed that Zn predominantly existed in an amorphous ZnO configuration (**Fig. S24-S25**). This conclusion was corroborated by the absence of crystalline ZnO features in HRTEM characterization, which aligned with the amorphous structural characteristics identified through spectroscopic studies (**Fig. S16**).

Note S2 Effects of Fe^{3+} on microstructure and composition of monometallic MOF Systems

To further elucidate the influence of Fe^{3+} incorporation on the structural and compositional of monometallic MOFs and their derivatives, four distinct ZIFs, including monometallic MZ-Z and MC-Z, along with bimetallic FZ-Z and FC-Z systems added with 2.4 mmol of Fe^{3+}, were systematically synthesized under identical conditions. Comparative analyses, as shown in **Fig. S8-S10,** revealed that the

incorporation of Fe^{3+} led to significant alterations in the crystalline structure and chemical composition of the MZ-Z precursor. Post-pyrolysis characterization revealed the presence of diffraction signatures associated with the $Fe_3ZnC_{0.5}$ and metallic Fe phase. This phase evolution suggested that in the absence of competitive ligand coordination from Co^{2+}, Fe and Zn underwent direct alloying processes that preferentially formed the thermodynamically favored $Fe_3ZnC_{0.5}$ phase during high-temperature treatment. Furthermore, the preferential coordination of Fe^{3+} with 2-MIM triggered a structural, topological transition in the MZ, transforming from a porous block configuration to a stabilized dodecahedral morphology. During subsequent pyrolysis, the Fe-dominated reinforced framework synergized with its catalytic induction effect on oriented carbon growth, enabling the MZ precursor (which underwent structural collapse into porous nanosheets) to evolve into an FZ that retained the polyhedral architecture of the parent framework.

In the MC and FC composite systems (**Fig. S11-S13**), the introduction of Fe^{3+} induced minimal crystal structure alterations in the precursor framework. However, the characterization of pyrolyzed derivatives displayed the emergence of a distinct metallic Fe phase, accompanied by marked attenuation in diffraction peak intensities corresponding to the metallic Co phase. These observations suggested that the insufficient heat treatment temperature, coupled with the confinement effect from the amorphous carbon matrix, collectively suppressed the formation of Fe-Co alloy phases, thereby limiting the reduction process to Fe^0 generation. Mechanistically, the introduced Fe species could act as grain growth inhibitors, reducing Co crystallite dimensions through Zener pinning effects while inducing lattice strain via substitutional/interstitial defects, which disrupted the long-range periodicity in the Co matrix and macroscopically manifested as diffraction peak broadening. The MC-Z precursor displayed an irregular leaf-like morphology with a certain thickness. Upon pyrolysis, this architecture underwent rapid structural collapse into aggregated clusters, attributed to the generation of detrimental gaseous byproducts (e.g., NO_x species) and the absence of Fe stabilization. The introduction of Fe species modulated the coordination environment of Co centers, thereby suppressing anisotropic growth

tendencies responsible for leaf-like formations. The FC composite maintained the morphology of the parent FC-Z precursor during subsequent thermal processing. Notably, the structural evolution characteristics of Co-based monometallic MOF exhibited remarkable similarity to those observed in Co/Zn bimetallic systems, thereby providing indirect evidence for the predominant coordination capability and reduction activity of Co centers within the bimetallic framework. In summary, Fe^{3+} incorporation can effectively control the synthesis of phases and structures in monometallic MOF systems by modulating the coordination environment, enhancing the coordination nodes, and establishing a reduction hierarchy.

Note S3 Analysis of hot field regulation results

Thermal field modulation was strategically implemented to further precisely manipulate the electromagnetic responsiveness of FCZ4 through systematic variation of pyrolysis temperatures. The relatively low temperature of 500 °C failed to provide an adequate thermodynamic driving force for substantial structural evolution, resulting in the microstructure of FCZ4-5 retaining its self-assembled configuration, as directly evidenced by the attenuation of diffraction peak intensities observed in the corresponding XRD (**Fig. S27**). Elevated temperatures within the 700-1000 °C range significantly enhanced carbon atom diffusion kinetics, thereby facilitating the structural reorganization of carbon matrices into graphitized configurations with improved crystallographic ordering. This was evidenced by the reduction in full width at half maximum and the intensity enhancement of characteristic graphitic carbon diffraction peaks observed in XRD. Concurrently, the formation of CNTs preferentially occurred at material surfaces, and the resulting nanotube network built spatial steric hindrance effects that substantially inhibited structural tailoring and reorganization processes within the materials. Moreover, the emergence of Co_7Fe_3 (PDF#50-0795) diffraction peaks became evident when the temperature exceeded 900 °C, offering evidence that corroborated the formation mechanism of Fe-Co solid solutions during low-temperature synthesis stages. Progressive elevation of the annealing temperature induced a significant improvement in atomic diffusion activation energy within the

system, which drove an ordered phase transformation within the solid solution. This demonstrated that thermal gradients exerted a critical governing influence over phase evolution pathways in composites.

The diminished EMW absorption efficiency observed in FCZ4-5 can be primarily attributed to the insufficient graphitization of the carbon matrix under low-temperature synthesis conditions, which resulted in a reduced dielectric loss capacity (**Fig. S54**). In contrast, elevated temperatures promoted the establishment of a continuous conductive network within the material matrix, substantially enhancing the complex permittivity. This phenomenon triggered a severe impedance mismatch at the material-electromagnetic wave interface, obstructing the subsequent efficient dissipation of electromagnetic energy. However, the synthesized composites, which exhibited pronounced temperature-dependent dielectric properties, were strategically engineered for high-performance electromagnetic shielding (EMI) applications. Surprisingly, the EMI effectiveness displayed temperature-dependent enhancement characteristics, with composite FCZ4-10 demonstrating superior performance by achieving a maximum total shielding efficiency of 66.94 dB (**Fig. S55**). This thermal-responsive behavior revealed that controlled thermal modulation effectively governed the dielectric response mechanisms of the material. As a result, it enabled dual-function switching between EMW absorption and shielding modes, advancing the development of multifunctional EMW management materials through temperature-mediated property control.

Note S4 Analysis of DFT calculation results

The formation energy of each material was determined through geometry optimization under consistent computational parameters. For the Fe-Co solid solution, Co_3ZnC, and $Fe_3ZnC_{0.5}$ systems, the final formation energies were calculated by first subtracting the formation energies of constituent free atoms, followed by comparing them in normalized per-atom or per-formula-unit formation energies. This approach effectively eliminated systematic errors arising from supercell size effects while maintaining comparability across different crystalline configurations. Based on the

XPS analysis, which revealed a progressive increase in Fe^{3+} content accompanied by the Fe/Co atomic ratio approaching 1:1, a 2×2×2 supercell of Co was constructed and subsequently subjected to doping with randomly distributed Fe atoms. The final formation energy results were summarized in **Table S5**. Computational analysis revealed that the Fe-Co solid solution phase exhibited substantially lower formation energy than the Co_3ZnC and $Fe_3ZnC_{0.5}$ phases. This energetically favorable configuration thermodynamically stabilized the Fe-Co solid solution as the dominant phase upon Fe^{3+} incorporation, demonstrating superior phase stability over competing compounds. Notably, when Fe atoms were doped in a disordered manner up to a 50% concentration (i.e., $Fe_{16}Co_{16}$), the system manifested increased structural complexity characterized by pronounced lattice distortion and localized atomic clustering. Such structural disorder generated heterogeneous stress distribution within the crystalline matrix directly correlated with a dramatic rise in formation energy. Therefore, these results confirmed that the Fe-Co solid solution phase was preferentially nucleated and stabilized within the trimetallic MOF architecture while simultaneously exerting dominance over the subsequent phase transformation pathways.

First-principles calculations on the pure Co system revealed a higher density of electronic states in the spin-down channel than the spin-up channel, indicating more substantial spin-polarized band dispersion in the former (**Fig. S29a** and **S30a**). In ferromagnetic Co, exchange interactions induced spin-polarized splitting of 3*d* orbital energy levels into spin-up and spin-down channels. The $3d^7$ electronic configuration of Co resulted in near-complete occupancy of spin-up *d*-orbitals, with filled states primarily situated below the Fermi level. In contrast, spin-down *d*-orbitals demonstrated partial occupancy, exhibiting electronic states proximal to the Fermi energy. This partial filling manifested as enhanced band dispersion within the spin-down channel, yielding a higher density of states near the Fermi level than the spin-up channel. This electronic structure characteristic also presented in Fe systems, reflecting fundamental principles governing ferromagnetic materials (**Fig. S33**).

The densification of spin-down energy bands exhibited a pronounced enhancement correlated with incremental Fe doping concentrations (**Fig. S29b-f**). This

was mainly attributed to the following: i) The spin polarization was further exacerbated by the $3d^6$ electron configuration of Fe and its stronger local magnetic moment. Upon Fe doping, the hybridization between Fe and Co strengthened the exchange interaction, inducing a marked splitting of the energy levels in the spin-down channel. This shifted the unoccupied states closer to the Fermi level, thereby increasing the density of the spin-down energy band as the Fe content rises. ii) The 3*d* orbitals of Fe exhibited hybridization with Co's 3*d* orbitals, with particularly pronounced interactions in the spin-down channel. This orbital hybridization induced a characteristic splitting of energy bands into distinct bonding and antibonding states. The bonding states, predominantly composed of spin-up configurations, were stabilized at lower energy levels positioned below the Fermi level. Conversely, antibonding states, primarily characterized by spin-down, occupy higher-energy states near or crossing the Fermi level. Notably, the antibonding states demonstrated a higher density of states (DOS) and exhibited progressively enhanced hybridization with increasing Fe concentration (**Fig. S30-S32**). This intensifying interaction introduced greater complexity to the spin-down band structure through two primary mechanisms. First, Fe doping introduced additional unoccupied d-orbitals, which generated supplementary unoccupied states in the spin-down channel via orbital hybridization. Second, these hybridized states facilitated energy band crossover phenomena and reduced electronic state degeneracy, ultimately manifesting as an enhanced density of states near the Fermi level. iii) The atomic radii of Fe (≈1.24 Å) and Co (≈1.25 Å) were nearly identical; however, doping Fe with Co introduced local lattice distortions characterized by variations in bond lengths or angles. These structural perturbations lowered the crystal symmetry, which in turn diminished the simplicity of the electronic band structure. In such a low-symmetry environment, initially, degenerate energy levels underwent further splitting, generating additional sub-bands. This phenomenon was particularly pronounced in the spin-down channel, where symmetry reduction amplified the complexity of the electronic states.

The total DOS exhibited a slight decline with increasing Fe doping concentration. This trend was attributed to localized lattice distortions induced by Fe incorporation,

which disrupted the crystalline symmetry and generated structural heterogeneity. Such atomic-scale modifications promoted the dispersion of electronic states, resulting in a measurable reduction of peak DOS intensities. Notably, this electronic structure modulation became most significant at intermediate doping levels (50% Fe substitution, $Fe_{16}Co_{16}$), where the synergistic effects of lattice strain and symmetry breaking reached optimal manifestation. Furthermore, the d-orbitals constituted the primary contribution to the total DOS, arising from the combined d-orbital contributions of Co and Fe. The spin-down channel maintained its dominance at the Fermi level, a characteristic that aligned with the electronic band structure analysis. Intriguingly, the projected density of states (PDOS) of Co exhibited a progressive decrease, whereas that of Fe demonstrated a concurrent enhancement. These mutually counteracting trends effectively mitigated substantial variations in the total DOS, maintaining its overall stability.

In the PDOS analysis of Fe and Co, the spin-up channel dominated the low-energy regime (-7 to -1 eV), characterized by fully occupied bonding states with strong d-orbital localization. Conversely, the spin-down channel exhibited partial d-orbital occupation due to spin-polarization effects, manifesting as an intense DOS peak near the Fermi level. This spin-asymmetric electronic structure resulted in spin-down states governing the electronic behavior at the Fermi energy. The 3*d* orbitals of Fe underwent hybridization with the 3*d* orbitals of Co, with the Fe d-orbitals exhibiting stronger electron localization and enhanced spin polarization, positioning them closer to the Fermi level. This electronic configuration resulted in a progressive intensification of the PDOS for the Fe 3*d* orbitals within the hybridized system. While the bonding states of Co in the low-energy regime and the antibonding states near the Fermi level remained dominant contributors, the overall PDOS for Co exhibited a slight reduction. This attenuation primarily stemmed from two concurrent mechanisms: i) partial electron transferred from Co's *d*-orbitals to Fe-Co hybridized states, and ii) the emergence of a pronounced density of states peak near the Fermi energy level, predominantly formed by antibonding states derived from Fe. The gradient in charge distribution at the Fe-Co hybrid interface established a pronounced dipole moment, facilitating polarization

relaxation processes at the interfacial region and enhancing dielectric loss characteristics.

The electronic band structures and DOS of Co_3ZnC and $Fe_3ZnC_{0.5}$ were also studied using the same calculations (**Fig. S34-S35**). Computational results demonstrated that $Fe_3ZnC_{0.5}$ possessed flatter energy bands near the Fermi level compared to Co_3ZnC, coupled with a significantly enhanced DOS peak in this critical energy region. These distinct electronic features, specifically the reduced band dispersion and elevated density of electronic states at the Fermi level, implied a greater population of charge carriers contributing to electrical conduction in $Fe_3ZnC_{0.5}$. This fundamental understanding of electronic behavior provided a theoretical explanation for the experimentally observed progressive improvement in electrical conductivity across the FCZ4 and FCZ5 systems.

Note S5 Python code for fitting the Havriliak-Negami model

```
import numpy as np
import matplotlib.pyplot as plt
from scipy.optimize import curve_fit
import pandas as pd

file_path = input("Input .xlsx file path: ")
S1 = pd.read_excel(file_path, header=None).to_numpy()
f = S1[:, 0]
e_real_data = S1[:, 1]
e_imag_data = S1[:, 2]

def epsilon(params, f):
    return params[0] + (params[1] - params[0]) / ((1 + (1j * 2 * np.pi * f * params[2]) ** params[3]) ** params[4]) - 1j * params[5] / (2 * np.pi * f * 0.008854)

#Users can set initial values here (x1, x2, x3, x4, x5, x6).
```

```
initial_guess = [x1, x2, x3, x4, x5, x6]
lb = [0, 0, np.finfo(float).eps, 0, 0, np.finfo(float).eps]
ub = [50, 100, 10, 1, 1, 100]

error_threshold = 5

def fit_func(f, epsilon_inf, epsilon_s, tau, alpha, beta, sigma):
    params = [epsilon_inf, epsilon_s, tau, alpha, beta, sigma]
    eps = epsilon(params, f)
    return np.concatenate([np.real(eps), np.imag(eps)])

params_fit_int = initial_guess
error_real = np.inf
error_imag = np.inf

for iter in range(100):
popt, _ = curve_fit(lambda f, *params: fit_func(f, *params), f, np.concatenate([e_real_data, -e_imag_data]),
    p0=params_fit_int, bounds=(lb, ub))
fitted_epsilon_real = abs(np.real(epsilon(popt, f)))
fitted_epsilon_imag = abs(np.imag(epsilon(popt, f)))
error_real = np.sum(np.abs(fitted_epsilon_real - e_real_data)) / np.sum(np.abs(e_real_data)) * 100
error_imag = np.sum(np.abs(np.abs(fitted_epsilon_imag) - e_imag_data)) / np.sum(np.abs(e_imag_data)) * 100
print(f'Current iteration count: {iter + 1}')
print(f'Real error: {error_real:.4f}%')
print(f'Imag error: {error_imag:.4f}%')
if error_real < error_threshold and error_imag < error_threshold:
    print('The fitting accuracy has reached below 5%, stop fitting')
```

```
            break
epsilon_inf_fit, epsilon_s_fit, tau_fit, alpha_fit, beta_fit, sigma_fit = popt

        print(f'Fitted epsilon_s: {epsilon_s_fit}')
        print(f'Fitted epsilon_infinity: {epsilon_inf_fit}')
        print(f'Fitted tau: {tau_fit}')
        print(f'Fitted alpha: {alpha_fit}')
        print(f'Fitted beta: {beta_fit}')
        print(f'Fitted sigma: {sigma_fit}')

        # Real
        plt.subplot(2, 1, 1)
        plt.plot(f, e_real_data, 'bo', label='Exp')
        plt.plot(f, fitted_epsilon_real, 'r-', label='Fit')
        plt.legend()
        # Imaginary
        plt.subplot(2, 1, 2)
        plt.plot(f, e_imag_data, 'bo', label='Exp')
        plt.plot(f, fitted_epsilon_imag, 'r-', label='Fit')
        plt.legend()
        plt.tight_layout()
        plt.show()
```

References

1. Jia H, Duan Y, Chen W, Di J, Wang M (2024) Multi-dimensional nano-microstructures design of MOF-derived $CoSe_2$@N-C composites toward excellent microwave absorption. Mater Today Phys 43:101415. https://doi.org/10.1016/j.mtphys.2024.101415
2. Tan R, Bai W, Yan J, Geng L, Jiang S, Guo R (2024) Flexible CoNiZn@Ti_3CNT_x MXene@carbon fabrics with hierarchical structure for efficient electromagnetic wave absorption. Chem Eng J 500:157444. https://doi.org/10.1016/j.cej.2024.157444
3. Zhang Y, Tian Y, Xu N, Cui P, Guo L, Ma J, Kang Y, Qin L, Wu F, Zhang L, Huang W (2025) In situ mechanical foaming of hierarchical porous MoC for assembling ultra-light, self-cleaning, heat-insulation, flame-retardant, and infrared-stealth device. Adv Funct Mater 35(6):2414910. https://doi.org/10.1002/adfm.202414910
4. Li K, Han L, Wang T, Zhang J, Cheng J (2024) 4D printing MOF-derived/multi-fluorination nanocomposites for ultra-efficient electromagnetic wave absorption and robust environment adaptivity. J Mater Chem A 12(11):6302-6317. https://doi.org/10.1039/d3ta06898f
5. Lou Y, Li J, Li X, Zhu Z, Shi Z, Xu B (2024) Single-atom Zn confined in hierarchical hollow microstructure as an acid/base-resistant microwave absorption materials. Nano Res 17(8):6785-6794. https://doi.org/10.1007/s12274-024-6689-z
6. Li L, Liu J, Pan F, Qiao J, Zhang X, Lin J, Liu W, Wu Q, Tao S, Wu F, Zeng Z (2024) Structural engineering of rare earth metal-organic frameworks derivatives with high anisotropy for high-efficiency electromagnetic wave absorption. Chem Eng J 481:148383. https://doi.org/10.1016/j.cej.2023.148383
7. Chen Y, Rao H, Wang B, Jin W, Nan K, Wang Y (2024) Hierarchical multi-interface $Co_{1-x}S/Co_9S_8$@C hollow microsphere for enhancing dielectric polarization as an efficient microwave absorber. Carbon 229:119475. https://doi.org/10.1016/j.carbon.2024.119475
8. Wang R, He Y, Tang C, Wu X, Zhuang Q, Liu X, Liu X, Zuo P (2024) Constructing crystalline/amorphous heterojunction in FeCo@C nanoboxes for enhanced

electromagnetic wave absorption. Carbon 229:119494. https://doi.org/10.1016/j.carbon.2024.119494

9. Liu G, Zhu P, Teng J, Xi R, Wang X, Wang X, Yan M, Wu C (2025) Optimizing MOF-derived electromagnetic wave absorbers through gradient pore regulation for Pareto improvement. Adv Funct Mater 35(18):2413048. https://doi.org/10.1002/adfm.202413048
10. Wu S, Wang C, Tang Y, Jiang J, Jiang H, Xu X, Cui B, Jiang Y, Wang Y (2024) Meta-organic framework-derived hierarchical Cu_9S_5/C nanocomposite fibers for enhanced electromagnetic wave absorption. Adv Fiber Mater 6(2):430-443. https://doi.org/10.1007/s42765-023-00362-9
11. Qiao J, Song Q, Zhang X, Zhao S, Liu J, Nyström G, Zeng Z (2024) Enhancing interface connectivity for multifunctional magnetic carbon aerogels: An in situ growth strategy of metal-organic frameworks on cellulose nanofibrils. Adv Sci 11(19):2400403. https://doi.org/10.1002/advs.202400403
12. Zhang X, Yao K, Wang X, Wang J, Guo H, Ma X, Yang Y, Wu H, Lu W (2024) Phytic acid-assisted hybrid engineering of MOF-derived composites for tunable electromagnetic wave absorption. J Mater Sci Technol 186:164-173. https://doi.org/10.1016/j.jmst.2023.10.054
13. Guo Y, Duan Y, Liu X, Tian J, Wen N, Fan Z, Pan L (2024) Construction of rGO/MOF-derived CNTs aerogel with multiple losses for multi-functional efficient electromagnetic wave absorber. Carbon 230:119591. https://doi.org/10.1016/j.carbon.2024.119591
14. Zheng J, Xu C, Li Z, Gu C, Li X, Li Z, Li Y, Lou G, Chen Y (2024) Growing bimetallic CoNi-MOF derivatives between MXene layers with hierarchically coral-like interfaces for enhanced electromagnetic wave absorption. J Mater Chem A 12(42):29103-29112. https://doi.org/10.1039/d4ta05088f
15. Wu X, Lin J, He Y, Wang R, Zhou Y, Qi H, Chen Y, Zuo P, Liu X, Zhuang Q (2024) Revealing electrostatic-manipulated self-assembly mechanism helps to readily design enhanced MOF-derived microwave absorbers. Carbon 227:119289. https://doi.org/10.1016/j.carbon.2024.119289

16. Qiao J, Song Q, Xuan L, Liu J, Zhang X, Zheng S, Lin J, Cai W, Zhang Q, Zeng Z, Wu N (2024) Dual cross-linked magnetic MXene aerogel with high strength and durability enables multifunctionality. Adv Funct Mater 34(33):2401687. https://doi.org/10.1002/adfm.202401687
17. Wang P, Fan D, Gai L, Hu B, Xu P, Han X, Du Y (2024) Synthesis of graphene oxide-mediated high-porosity Ni/C aerogels through topological MOF deformation for enhanced electromagnetic absorption and thermal management. J Mater Chem A 12(14):8571-8582. https://doi.org/10.1039/d4ta00125g
18. Sun C, Lan D, Jia Z, Gao Z, Wu G (2024) Kirkendall effect-induced ternary heterointerfaces engineering for high polarization loss MOF-LDH-MXene absorbers. Small 20(48):2405874. https://doi.org/10.1002/smll.202405874
19. Sun K, Xie Z, Yang X, Long Y, Yang P, Cheng C, Qi X (2025) Enhanced microwave absorption in C@Co/carbonyl iron fiber composite with multi-level interfaces. Adv Compos Hybrid Mater 8(1):29. https://doi.org/10.1007/s42114-024-01124-w
20. Yan J, Bai W, Cui C, Jiang S, Wang W, Tang H, Guo R (2024) Metal-organic framework-derived lilac flower-like CoNiZnO@nitrogen-doped carbon composites via a trapping microwave strategy for efficient absorption. J Mater Chem A 12(42):28794-28804. https://doi.org/10.1039/d4ta05222f
21. Sun R, Ming X, Yan G, Wang L, Cheng J, Zhang X, Li D, Li H, Li Z, Chen J, Wu Y (2024) Efficient nanofibrous electromagnetic wave absorber inspired by spider silk hunting. Small 20(52):2407178. https://doi.org/10.1002/smll.202407178
22. Weng J, Liu Y, Huang X (2025) Synthesis of in situ grown CNTs on MOF-derived Ni@CNT with tailorable microstructures toward regulation of electromagnetic wave absorption performance. Carbon 231:119678. https://doi.org/10.1016/j.carbon.2024.119678
23. Hou Z, Zhang M, Kong L, Fang H, Li Z, Zhou H, Jin H, Cao M (2013) Microwave permittivity and permeability experiments in high-loss dielectrics: Caution with implicit Fabry-Pérot resonance for negative imaginary permeability. Appl Phys Lett 103(16):162905. https://doi.org/10.1063/1.4825378

24. Liu Y, Zhou J, Li C, Zhang H, Wang Y, Yan Y, Duan L, Cheng Z, Ma Y, Yao Z (2025) Interfacial coupling effects in two-dimensional ordered arrays for microwave attenuation. Nat Commun 16(1):202. https://doi.org/10.1038/s41467-024-55776-9